

Atmospheric NO_x removal: study of cement mortars with iron- and vanadium-doped TiO₂ as visible light–sensitive photocatalysts

M. Pérez-Nicolás^a, I. Navarro-Blasco^a, J.M. Fernández^a, J.I. Alvarez^{a*}

^aUniversidad de Navarra, Facultad de Ciencias, Departamento de Química, MIMED Research Group.

Irunlarrea, 1. 31008 Pamplona, Spain

Available at : <http://dx.doi.org/10.1016/j.conbuildmat.2017.05.132>

Abstract

Mortars made with Portland cement, two different calcium aluminate cements and air lime were chosen to incorporate photocatalytic additives, because they have large exposed surfaces that boost the photochemical oxidation (PCO) of atmospheric pollutants such as nitrogen oxides. TiO₂ as reference catalyst, and two doped titania, Fe-TiO₂ and V-TiO₂, which were expected to increase the sensitivity of the additives towards the visible light, were studied. Cementing matrices, particularly air lime and high alumina cement mortars, yielded significant amounts of NO removal under the three illumination conditions studied (UV, solar and visible light), with high selectivity response for NO abatement (up to 60 to 80%) and low NO₂ release. The presence of calcium carbonate has been shown to have a synergistic effect, enhancing the PCO of these mortars under different light sources.

1. Introduction

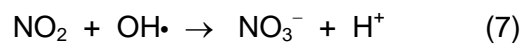
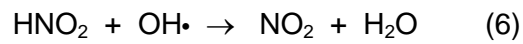
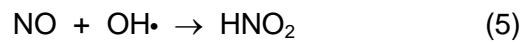
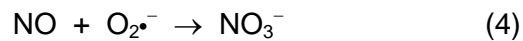
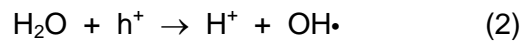
Atmospheric pollution is one of the most severe problems that scientific community has to face up. Industrial activity is responsible for the presence of toxic gases in the atmosphere. Regarding the chemical composition of these pollutants, nitrogen oxides NO_x ($\text{NO} + \text{NO}_2$) have been recognised as potential agents causing respiratory diseases and acid rain [1]. In order to remove NO_x from the atmosphere, photochemical oxidation (PCO) has been developed in different systems by means of the use of photocatalysts.

Photocatalysts can be immobilized into cementitious materials with the aim of enhancing their activity and developing applications in new areas. Cement-based materials offer a large ratio of fixation sites for the photocatalysts, as well as extensive exposure surfaces and have been reported as target supports of these photocatalysts [2-7]. These modified materials have been proved to be efficient to depollute the environment by degrading NO_x (De NO_x effect) [8-10]. Furthermore, photocatalysts can give rise to an increase of the hydrophilicity of the surfaces since they are known to generate photo-induced superhydrophilicity. This point is related to the self-cleaning ability of these surfaces. This ability is based on the synergy of two properties: by one hand, the photo-induced oxidation of the adsorbed organic compounds and, by the other hand, the photo-induced super-hydrophilicity [11]. As main responsible for the stains on the surface of building materials literature has pointed out to composites including organic compounds, such as fatty acids and hydrocarbons, that can trap dust and atmospheric particles [11]. For hydrophilic surfaces water drops spread over the surface and form a film of water (initially water is chemisorbed onto the surface of the photocatalyst; then, the thickness of the layer is increased because these water molecules adsorb water by physisorption, either by van der Waals forces or by hydrogen bonds) [12]. This film of water will act as a barrier to prevent the close contact between the surface of the building material and the pollutants. Pollutants close to the surface of the material will be easily removed by this loose water barrier. Therefore, during the process of spreading of water drops, the contaminants on the surface are washed away [13].

For mortars with photocatalysts, water contact angle is expected to decrease making surfaces easily washable by rain water and preventing dirt from accumulation, according to the aforementioned reasons. These building materials would be self-cleaning surfaces [14-17]. This fact reduces the cleaning maintenance costs, obtaining an environmentally friendly material [18-19].

Semiconductor metal oxides are commonly used as photocatalysts in PCO reactions [20]. Semiconductors have an electronic structure characterized by a filled valence band and an empty conduction band. When the energy provided by a photon (light source) matches or exceeds the band gap, one electron overcomes the energy barrier and is promoted from the valence band to the conduction band, leaving a hole (positively charged) in the valence band [21]. In the presence of air and oxygen, pollutants -that are adsorbed on the semiconductor surface-, may undergo photo-oxidation.

The most common photocatalyst used in building materials is TiO₂. The PCO chain reaction of the NO_x removal by TiO₂ has been generally accepted as follows [7]:



Titanium is an excellent photocatalyst under UV light. Nevertheless, outdoor radiation only presents a minor 4-5% of UV photons [22]. Different attempts to improve the sensitivity of titanium towards photons of the visible light spectrum have been carried out [23-25]. Among

these strategies, the doping of TiO_2 with transition metals (Fe, V, Cr...) has shown to be useful [25-27] and will be employed in this work.

Although usually ordinary Portland Cement, PC, has been studied as the main building material acting as support of TiO_2 , previous studies have also shown the potential usefulness of cementing matrices based on calcium aluminate cement (CAC) to support bare TiO_2 . Different behavior was found for high alumina cements, HAC (iron-lean calcium aluminate cements) and cements with a high amount of ferrite phase (iron-rich calcium aluminate cements, so called low alumina cements, LAC), the first ones being the most effective in the NO_x removal. This efficiency was related to a good ability for NO_2 sorption: the incidence of UV illumination gave rise to the formation of holes on calcium aluminates (Lewis acid sites) that preferentially interacted with the Lewis base NO_2 [28]. However, the effect of other photocatalysts with expanded sensitivity towards visible light on the atmospheric NO_x removal has not yet been tackled in these calcium aluminate cements.

On the other hand, lime-based materials for construction purposes have shown a growing development over the last years [29-31]. Lime mortars, in monolayer as well as in renders, could also be an interesting supporting binder for these active agents, but this topic remains almost unexplored in the literature [32].

Chemical composition, heterogeneity and pore structure of the supporting materials can have a strong influence on the PCO activity [7,20]. Synergistic effects improving the atmospheric NO_x removal efficiency have been reported in different systems leading, for example, to a precise separation between active sites which reduces the electron-hole recombination rates [32-35].

The present work aims to explore the use of photocatalytic additives with expanded sensitivity towards visible light radiation in four different binding materials (PC, two calcium aluminate cements, HAC and LAC, and air lime-based mortars) to remove atmospheric NO_x gases. The outcome of this research could be useful to apply new depolluting building materials that would be active under different illumination conditions, particularly in exposed areas with low sunlight

illumination (where the scarce UV component is further restrained). Three nanostructured photocatalytic additives were used for the obtaining of the active mortars: bare TiO_2 , which was used for comparative purposes, and two different doped TiO_2 , Fe- TiO_2 and V- TiO_2 . De NO_x activity of these mortars was assayed under three distinct radiation types, namely UV, solar and visible radiation, in order to investigate the real effect of the doped additives in these binding matrices. Attention will be also focused on the release of harmful NO_2 as intermediate product of the PCO of the NO: for depolluting building materials, a complete NO photo-oxidation until nitrates (which can be rain-washed) would be desirable in order to effectively reduce the atmospheric pollution. The efficiency of these new photocatalytic cementing matrices in terms of NO_x (considering NO removal and NO_2 release) vs. NO degradation will be assessed. Finally, the hydrophilicity of the mortars is also monitored by the static water contact angle, as an indicator of the potential self-cleaning ability of these mortars.

2. Experimental section

2.1. Materials

Four different binders were used to prepare the mortars:

- a) Portland Cement (PC) (type CEM II32.5 N, Portland),
- b) High alumina cement (HAC) (Ternal White, Kerneos)
- c) Low alumina cement (LAC) (EN 14647 CAC, Ciments Molins Industrial)
- d) Dry slaked lime (class CL 90-S according to European standard [36], CALINSA, Spain).

Chemical and mineralogical compositions, obtained by X-ray fluorescence (XRF) and X-ray diffraction (XRD), of the binders are summarized in Table 1. A siliceous aggregate was also used: its mineralogical composition and grading has been reported elsewhere [37].

Three photocatalysts were used: bare TiO_2 (Aeroxide P25, Evonik) and Fe- TiO_2 and V- TiO_2 (synthesized by flame spray pyrolysis, FSP [27], and supplied by Centro Tecnológico

L'Urederra, Spain). According to the data provided by the supplier, Fe-TiO₂ was obtained by a solution of Fe³⁺ ion as precursor, whereas V-TiO₂ was obtained from a V₂O₅-TiO₂ mixture.

2.2. Characterization of the photocatalytic additives

Specific surface area was determined in samples by the BET method (ASAP 2020 equipment, Micromeritics) studying N₂ adsorption at 77K. XRD and XRF were used to study the mineralogical and chemical composition of the additives. Table 2 summarizes the experimental specific surface values obtained for bare titania and doped additives. Particle size of the crystallites was determined according to the Scherrer equation from the XRD results (Table 2) [38]. Anatase and rutile appeared as the only crystalline compounds in all samples (Fig. 1a).

The surface chemical composition of the powders was investigated by quantitative studied of X-ray photoelectron Spectroscopy (XPS) (Equipment ESACALAB 200-X with ECLIPSE data-system (VG Scientific) and MgK-alpha excitation). Survey spectra are depicted in Fig. 2a. The assessment of the O 1s region (Fig. 2b) was conducted using Gaussian values to decompose the different contributions of the peak. The resolution of this area provided three different peaks (in Fig. 2b indicated as I, II and III). Peak I in the Figure is attributed to the crystal lattice oxygen in the oxide, Ti-O (529.5 eV) in TiO₂ whereas the assignment of the second one (II, 531.5 eV) was related to the Ti-OH. Experimental results showed that the doping of the titania lattice with either Fe or V caused an enlargement and widening of this second peak [39].

XPS spectra, in Fig. 2d, also showed peaks related to V2p 3/2 and V2p 1/2, which appeared at 515.8 and 523.7 eV, respectively [27]. These peaks are mainly related to the presence of V⁴⁺ [40-43]. The absence of a shift of the anatase (1 0 1) peak (Fig. 1b) in XRD pattern proved that there is no V⁴⁺ incorporation into the TiO₂ lattice [40-42]. Considering these data, the very low solubility of vanadia in TiO₂ and the precursors used in the FSP synthesis, vanadium located dominantly on the titania surface appears as the most probable structure. This agrees with the known fact that -in FSP processes- TiO₂ nucleates first, giving rise to a titania core, and then different vanadium compounds create a shell after their deposition on the titania surface [44-46], as we experimentally confirmed with their superficial detection by XPS. The vanadium

structures (generally VO_x) would be isolated monomeric vanadyl centers with V^{4+} according to the XPS results and to the low vanadium loading [44,47], since quantitative data (XRF) for V revealed the presence of 1% of V in the doped samples. Therefore, the vanadium-bearing additive can be characterized as heterostructures between TiO_2 and VO_x . For the sake of brevity, this additive will be called as V- TiO_2 .

For iron-doped titania, XPS spectrum in the region of 700 to 740 eV was unable to identify the peaks of Fe (Fig. 2e) due to the low concentration of dopant and the fact that XPS only characterizes the most outer surface of the samples [48]. By X-ray fluorescence, Fe- TiO_2 additive showed a percentage of 0.179 % for Fe. By XRD, we did not find evidences of secondary Fe_2O_3 phases. Furthermore, other changes in the XPS spectra, in XRD and considering also the chemical precursor used in the synthesis, suggest the definite incorporation of Fe into the TiO_2 lattice. The experimental evidences can be summarized as follows: (i) The chemical shift of the titanium peak $\text{Ti}2p\ 3/2$ in the XPS spectrum: from the stoichiometric TiO_2 lattice (458.1) to 459.1 for Fe- TiO_2 , proving some changes in the chemical bonding [48] (Fig. 2c). (ii) The increase in the hydrophilicity of the sample (OH adsorbed as proved by the second peak after deconvolution of the $\text{O}1s$, in the XPS results in Fig. 2b), in accordance with results of TiO_2 samples doped with iron [25]. (iii) The clear displacement of the anatase (1 0 1) XRD peak (see Fig. 1b, from $25.30^\circ\ 2\theta$ to $25.41^\circ\ 2\theta$), in good agreement with the reduction in the lattice parameters and a parallel shrinkage of the unit cell for low concentration of Fe dopant [49]. The presence in the titania lattice of Fe^{3+} in the low spin state, coordination 6, replacing Ti^{4+} (with higher ionic radius) is compatible with this XRD peak displacement. (iv) The enhancement in the percentage of rutile formation for Fe- TiO_2 (69.1% of anatase and 30.9% of rutile), as compared with 78.8% and 21.2% in bare TiO_2 (Table 2).

Therefore the characterization showed that the vanadium-bearing additive was a heterostructure between TiO_2 and VO_x (vanadyl centers) whereas in the case of the Fe-doped additive Fe^{3+} was found to substitute Ti^{4+} within the TiO_2 lattice.

The light absorbance of the photocatalysts was examined using a UV-2100 Shimadzu instrument. The UV-vis diffuse reflectance spectra were recorded in the wavelength range 300–

800 nm. The doped additives showed increased absorption within the visible region, evidencing that these compounds increased their sensitivity towards visible illumination as compared with bare TiO₂ (Fig. 3).

Surface charge and particle size distribution of the alkaline suspensions of the additives (1 wt. %) were determined using an electroacoustic-based zeta potential analyser (ZetaProbe, Colloidal Dynamics) and Malvern Nanozeta Sizer, respectively.

2.3. Mortar preparation and curing regimes

Samples were prepared with a binder:aggregate ratio of 1:3 by weight, which has been used in previous works. The binder:water ratio was adjusted in each fresh mortar in order to ensure a good workability (spread in the flow table test of 175 ± 10 mm) [50]. Three different concentrations of each photocatalyst (TiO₂, Fe-TiO₂ and V-TiO₂) were studied: 0.5 wt. %, 1 wt. % and 2.5 wt. % with respect to the binder weight.

Binder, aggregate and additives were blended for 10 min at low speed in a mixer. Water was then added and mixed for 90 s at low speed. Then, fresh state properties were determined as described below. Afterwards, mortars were cast in cylindrical moulds (40 mm of diameter and 36 mm of height) and de-moulded 24 h later (7 days later in the case of air lime samples). Curing conditions were as follows:

- PC moulds were cured at 20°C and 95 % RH (Relative Humidity).
- Mortars of calcium aluminate cements, HAC and LAC, were subjected to two distinct curing regimes: curing condition 1 was the same used for PC mortars, in which calcium aluminate cements are expected to develop metastable hydrates. Parameters for curing condition 2 were 60°C and 100% RH: under such conditions, calcium aluminate cements yield cubic, stable calcium aluminate hydrates and higher porosity [28].
- Air lime mortars were cured at 20 °C and 60% RH.

Considering the relatively low percentages of the additives, the final color of the prepared

specimens did not undergo any changes at naked eye after the additive incorporation.

2.4. Characterization of the mortars with photocatalysts

Pore size distributions (PSD) were obtained by mercury intrusion porosimetry (MIP) (Micromeritics-AutoPoreIV-9500; pressure 0.0015 to 207 MPa). Additional characterization by FTIR-ATR (Nicolet-Avatar 360, resolution of 4 cm^{-1}) was also done.

Microstructural examination and elemental mapping of the observed areas was carried out by Scanning Electron Microscopy combined with energy-dispersive X-ray microanalysis (SEM-EDS, FEI Instrument, Quanta 3D FEG, with INCA IE 350 Penta FET X-3 EDS, Oxford Instruments).

With the aim of evaluating the changes in the hydrophilicity of the mortars, the static water contact angle (WCA) was measured with mortars exposed to UV, solar and visible light. A video-based optical contact angle measuring instrument (OCA 15EC Dataphysics) was used. The reduction of the WCA could allow the dirt (oily smog, dust, carbonaceous particles ...) to be washout by rain. Surfaces with WCA between $0^\circ < \theta < 90^\circ$ are generally considered to be hydrophilic and when the WCA becomes less than 10° , it is considered superhydrophilic [13].

In all instances compressive strengths of the mortars were tested at different curing ages (28, 91, 182 and 365 days). Specimens with the photocatalytic additives showed enough mechanical resistances to allow the real application of the mortars and values after one curing year were generally above 30 MPa for PC samples, 35-40 MPa for HAC and LAC mortars and 1.5 MPa for air lime mortars.

2.5. Photocatalytic studies: DeNO_x ability

Photocatalytic activity was studied in a flow-through setup [51] onto discs of the samples (slices obtained from the cylindrical samples prepared as described in 2.3) of height 1 cm and diameter 4 cm and one year-curing old. The total exposed area of the discs was 25.14 cm^2 . A scheme can be seen in Fig. S1 of the Supplementary Information. Two different lamps were used as

irradiation source: Osram Ultravitalux 300W, for UV illumination, and Philips SON-T PIA Plus 250W, for solar and visible irradiation, with intensities of 43.4 W m^{-2} and 36.7 W m^{-2} measured, respectively, by a Traceable ultraviolet light meter Control Company (UV-A sensor 320-390 nm) and a Photo-Radiometer HD2302.0 Delta Ohm (visible sensor LP-471 RAD 400-1050 nm). For UV-A, these light intensities are in line with an average value of 35 W m^{-2} that has been reported for UV-A illumination (summer days in Central Europe) [52] and has been selected as a mean value of the UV-A light intensities (times close to noon, summer solstice, clear sky day) for subtropical regions including Southern Europe [53]. For solar light, the lamp provided around 10% of the intensity of the irradiation from 400-1050 nm determined for outdoor exposure in a sunny summer day (considering the solar constant as $1366 \pm 2 \text{ W m}^{-2}$ and the angle of incidence and the number of sunny hours, 342 W m^{-2} would be the average global power density at the top of the atmosphere. Just 70% reach the ground, so that an average value of 240 W m^{-2} can be estimated as the total solar irradiance (from which visible spectrum accounts for ca. 38-41% of the total irradiation). In order to achieve strict visible radiation a coloured glass filter (FGL420, Thorlabs) was used for solar radiation which cuts off completely wavelengths shorter than 410 nm. Experimental conditions were $50 \pm 10\% \text{ RH}$ and $25 \pm 2^\circ\text{C}$. The cylindrical photoreactor (height 12 cm; diameter 14 cm) was fed by a 500 ppb NO stream at a $0.78 \text{ L} \cdot \text{min}^{-1}$ flow. Concentrations of NO and NO₂ were determined by a chemiluminescence detector (Environnement AC32M). Conditions of the photocatalytic assays fall within the same order of magnitude used in similar experimental settings [7,28].

NO_x stream flowed over the sample in the dark for 10 min in order to stabilize NO concentration and to avoid the interference of the adsorption phenomena, which, together with the direct photolysis, were subtracted after running blank experiments for all tests. Then, the photoreactor was irradiated for 30 minutes. After that, the light was switched off and NO_x stream continued flowing over the sample 10 minutes more. (Fig. S2 in the Supplementary Information shows, as an example, one experimental profile of the NO_x abatement curves). Error analysis of the experimental results obtained by this method, as expressed in terms of

relative standard deviation, was calculated under reproducibility conditions to be 3.3% from replicate analysis of at least three identical samples. The performance of the photocatalytic additives in powder was studied under UV, solar and visible irradiation (Fig. 4). The positive effect of the doped structures was observed under solar and visible illumination (higher NO removal than bare TiO_2). The simultaneous presence of anatase and rutile, with formation of oxygen vacancies at the grain boundaries, accounts for the bare TiO_2 activity under strict visible irradiation [54].

3. Results and discussion

3.1. Role of the binding matrices in the NO_x removal

Results of the NO abatements of all tested mortars under UV, solar and visible irradiations were monitored (Fig. 5). The experimental results showed, in general, a dosage-dependant pattern: the higher the dosage of additive, the higher the percentages of NO abatement. There is no evidence supporting a drop in the effectiveness owing to a coupling electron-hole as a consequence of an excess of the photocatalytic additive in the mortars. This outcome is reasonable taking into account the relatively low maximum percentage of the additive used (2.5%) and its incorporation in bulk, which lead to a good separation between the particles of the additive.

As it can be inferred from the results, the use of photocatalysts in all instances greatly improved the performance of the controls (photocatalyst-free mortars). The NO removal observed in the control samples can be ascribed to adsorption phenomena, among which the disproportionation of NO due to the alkaline pH of the mortars may be highlighted [2].

Lime and HAC mortars, among all the binding matrices, showed the best values of NO abatement under UV, solar and visible light. For example, under UV light (Fig. 5a), percentages above 20% of nitric oxide removal were measured in many cases for these matrices. The good performance of high alumina cement with photocatalysts may be related to: (i) the sensitivity of the calcium aluminates towards illumination, acting as Lewis acid sites, as we established in a

previous work, in a better degradation of nitrogen oxides in high alumina cement mortars [28]; and (ii) the appropriate pore size distribution: HAC mortars exhibited a low amount of small pores (below 0.05 μm), favouring the gas intrusion in samples in comparison with PC mortars [7,55]. See, as an example, MIP curves of HAC mortars and PC mortars (in the latter case with a strong population of pores below 0.05 μm when photocatalysts were incorporated) (Fig. 6a and Fig. 6b). Cement mortars with a strong prevalence of nanopores (in this case meaning pores below 0.05 μm) have been seen to restrain the diffusion of the gaseous pollutants into the mortar structure, thus reducing their photocatalytic efficiency [55].

In the case of air lime mortars, the high nitric oxide removal rates might be explained taking into account the pore structure of these monolithic specimens, with a good interconnected structure evidenced by the critical pore size of these mortars (around 0.7-0.8 μm) and the almost unimodal pore size distribution (Fig. 6c). This critical pore size can be defined as the most common diameter that allows the maximum percolation through the interconnected pore network. NO molecules would be able to easily reach the inner parts of the air lime mortars, being adsorbed onto the photocatalytic active sites.

Furthermore, the availability of significant amounts of calcium carbonate in these mortars (both HAC and lime mortars) would be responsible for the reaction with nitric acid (final product of the NO photooxidation), yielding calcium nitrates that are easily removed from the photocatalyst surface thus enhancing the PCO reaction [33]. Otherwise, the formation of nitric acid on the surface of the photocatalyst (the rate limiting step [56]) would result in a deactivation of the compound [57]. The synergistic effect of calcium carbonate to improve the PCO efficiency of TiO_2 has already been mentioned in other works [33,58,59] as well as the positive effect of the simultaneous presence of TiO_2 and nanolime (colloidal nano-structured calcium hydroxide) [60].

In order to confirm these assumptions, selectivity (expressed in percentage) of the photocatalytic matrices was calculated ($\% \text{NO}_x$ removal $\times 100 / \% \text{NO}$ removal) as an estimation of the NO degraded that finally yields nitrate instead of the harmful NO_2 [61] (Table 3). Under

UV light, it can be observed that air lime mortars as well as HAC mortars showed the highest ratios as compared with PC or LAC mortars, generally well above 60% or even 70%. These selectivity percentages are outstandingly higher than other reported in the literature (ca. 50% for different photocatalysts [61]) and better than other immobilizing systems including photocatalysts [62], thus remarking the interest of these binding materials which present a favourable ability to yield catalytic materials with improved depolluting properties. These high selectivity values prove that both air lime and HAC mortars completely removed large percentages of NO until total oxidation without secondary and non-desirable release of large quantities of NO₂ [63]. Under solar and visible illumination sources, selectivity values for these mortars were very high (above 70% and even 80%) and the doped additives exhibited an increase in their selectivity performance. This finding supports the interest of these air lime and HAC mortars as matrices to achieve an effective depolluting performance of atmospheric environment, with very good rates of NO removal with a comparatively low release of NO₂, irrespective of the nature of light impinging on them.

FTIR-ATR examination of the tested mortars after conducting the NO_x abatement tests was also helpful to confirm the enhanced action mechanism of these air lime and HAC mortars, which involves a complete PCO of NO: the absorption band of calcium carbonate underwent a dramatic reduction as consequence of its intense consumption due to the reaction with nitric acid (as the final NO photooxidation product). As an example, Fig. 7a shows the FTIR spectra of air lime sample with TiO₂, before and after its exposure to NO (in which a prolonged 2 hours period was used in order to raise the intensity of the PCO reaction). A clear reduction of the CO₃²⁻ absorption bands at ca. 1425 cm⁻¹, 880 cm⁻¹ and 710 cm⁻¹ was observed. At the same time, and as a consequence of the acid-base reaction between the final PCO product (nitric acid) and calcium carbonate, new moderate bands appeared at 665 and 685 cm⁻¹, which were ascribed to the formation of hydrogencarbonate (HCO₃⁻) [59]. Small sharp band at 830 cm⁻¹ would be indicative of the traces of nitrates, since they correspond to v₂ vibration mode of the D3h ionic nitrates [64]. Some other weak signals could also be ascribed to nitrates: 730 cm⁻¹, v₄ vibration mode of the D3h ionic nitrates and 760 cm⁻¹ to the v₆ of the -ONO₂ group vibration (C2v).

Similar results were obtained in a HAC mortar (Fig. 7b), with a clear reduction of the absorption linked to the presence of carbonate group and with the appearance of two sharp bands at 685 and 760 cm^{-1} , ascribed to the HCO_3^- and nitrate formation. Comparatively, a sample of LAC mortar yielded much more attenuated changes (Fig. 7c). In Fig. 7b and 7c, the broad peak around 900 cm^{-1} can be related to the asymmetric stretching vibration of Al–O bonds of $[\text{AlO}_4]^-$ tetrahedra in C_3A and C_{12}A_7 [65].

When the influence of the source of illumination was considered, the efficiency in the NO removal of the UV light was found to be the highest, as can be observed by the percentages of NO degraded (Fig. 5). Under the solar illumination, all the values of NO removal were lower due, among other factors, to the lower irradiance provided by the light source. Solar light includes a small percentage (4.5%) of UV photons, but their effect in UV sensitive catalysts can usually outweigh the contribution of the visible light activity [26]. The experimental results under solar illumination showed a good agreement with those measured under UV light: the matrices (air lime and HAC mortars) with the highest NO removal under UV light also presented the highest NO removal under solar illumination. Results under strict visible illumination also yielded the highest values of NO degradation for these HAC and air lime binding matrices. In addition, LAC mortars (cured under condition 1) also showed noticeable ability for NO removal. The presence of doped TiO_2 increased the NO removal activity of the mortars under visible light. Considering the low irradiance of the lamp as compared with the sunlight irradiance, these results of NO removal would be expected to clearly increase in outdoor exposure.

However, this favourable DeNOx ability of these materials does not include the potential impact on the aesthetic appearance of the façades that should be further studied.

The NO removal reactions were adjusted to pseudo-first-order kinetics, in agreement with the expression $\ln(C_t/C_0) = -kt$, in which k is the apparent rate constant of disappearance of the nitrogen oxide, and C_0 and C_t are the initial and instant concentrations of NO, respectively [66]. The plotting of $\ln(C_t/C_0)$ vs. time of irradiation yielded a linear relationship. Table S1 in Supplementary Information collects the values of the kinetic constants of the linear adjustments.

From the results, it can be observed that the fastest systems were also the most efficient composites for the abatement of NO. Kinetics analysis showed that both lime and HAC mortars degrade NO at the highest rate. Other significant conclusion was that, under UV illumination, pristine TiO₂ was the additive yielding the swiftest processes whereas Fe-TiO₂ and V-TiO₂ showed somewhat sluggish activities. Under solar irradiation, HAC mortars with bare TiO₂ degraded NO at the highest rate, whereas air lime mortars showed relatively fast processes with the three tested additives.

3.2. Role of the doped additives in the photocatalytic activity

Under both solar and visible illumination, the mortars with the doped additives (Fe-TiO₂ and V-TiO₂) exhibited some differences that deserve a painstaking discussion from a mechanistic point of view. In general, the presence of Fe-TiO₂ favored the activity under solar and visible light for air lime mortars, while keeping a reasonably high level of efficiency for HAC mortars under the two different curing regimes. Under an illumination source including a visible light component, the broader sensitivity of V-TiO₂ generally improved the DeNO_x process, although samples usually yielded lower activity in comparison with Fe-TiO₂ (except for PC and LAC mortars).

After the doping process, the photocatalytic activity of the parent TiO₂ lattice may be modified owing to the formation of new energy levels between the valence band and the conduction band (CB). The increased sensitivity of the VO_x-TiO₂ heterostructures in the V-TiO₂ additive towards visible light (as proved by the bathochromic shift of the band gap energy) can be explained considering the good dispersion of vanadium oxide on TiO₂ (yielding monomeric vanadyl centers) and also the formation of a new energy level in the energy gap due to the d-orbital levels of these centers [47]. Therefore, the excitation of a 3d electron of the V⁴⁺ into the TiO₂ conduction band took place [67-68]. The trapped electrons would migrate to the TiO₂ surface and the adsorbed O₂ would be reduced to O₂⁻, while the hole migration would transform the surface hydroxyl group into hydroxyl radical (OH•) [23]. It should be noticed that NO_x photocatalytic oxidation is mediated essentially by the hydroxyl radical and, to a much lesser extent, by O₂⁻ [69,70].

Basically, the action mechanism of the Fe-TiO₂ would involve a charge transfer from the d orbital of Fe³⁺ to CB of TiO₂. A detailed mechanism for photogeneration of active species has been reported by Choi et al. [68]. For a complete consideration, the energy levels of the impurities for hole and electron traps are very important, but also the energy involved in the charge release and migration in the lattice plays a capital role. In a dual phase of active titania (anatase and rutile), the improvement in the photocatalytic effect due to the iron dopant has been ascribed to the reduction in the recombination rates, i.e., the efficiency of Fe-doping for separating electron-hole pair in TiO₂ [25].

It has been proven (see section 2.2.1) that, whereas vanadium appeared mainly on the TiO₂ surface as vanadyl V⁴⁺ centers (TiO₂-VO_x heterostructures), iron, as Fe³⁺, substituted Ti⁴⁺ within the titania lattice. Experimental results showed, in general, a better performance for Fe-TiO₂ samples than for V-TiO₂ samples, in spite of the fact that V-TiO₂ showed a more intense light-harvesting in the visible light spectrum (see Fig. 3). Different factors can be argued to explain this performance:

- 1) The different energy levels between Fe²⁺/Fe³⁺ or V³⁺/V⁴⁺ with respect to the CB of the titania lattice (Ti³⁺/Ti⁴⁺ level). The Fe²⁺/Fe³⁺ energy level is located very close to Ti³⁺/Ti⁴⁺ level, so that a trapped electron in Fe²⁺ can be quickly transferred to a nearby Ti⁴⁺, leading to a interfacial electron transfer [68].
- 2) At the same time, whereas V⁵⁺ (for the V⁴⁺/V⁵⁺ level) can only act as an electron scavenger, Fe⁴⁺ (for the Fe³⁺/Fe⁴⁺ level) can trap a hole with long lifetime, as a consequence of the immobilized electron in the Fe²⁺, as explained before [68]. The impact of the hole formation and the subsequent generation of the hydroxyl radical on the NO_x PCO has been mentioned, and Fe-doped titania then appears to be more effective for the NO_x removal.
- 3) The different exposure of active sites in the mortars. Given that PCO is a superficial phenomenon, specific surface of the additives as well as their real distributions in the mortars are of the utmost importance. Although V-TiO₂ has a higher specific surface than Fe-TiO₂, its trend to agglomerate in alkaline aqueous suspensions (a well-known

phenomenon for nano-materials) should be studied. To this aim, different experiments were carried out:

- a) First, zeta potential tests of the additives were executed. Particles in suspension (in this case achieved in the plastic state of the binding pastes) of relatively small surface charge, tend to agglomerate, reducing their exposed active sites. Particles with zeta potential values between +30 and -30 mV are considered to be unstable, with a strong tendency to form flocs. The used photocatalysts showed zeta potential values in alkaline aqueous suspension of +38.95 mV, +11.90 mV and +6.85 mV, for bare TiO₂, Fe-TiO₂ and V-TiO₂, in line with other reported values [71]. The zeta potential values of the two doped additives fall within the instability region and the V-TiO₂ is the additive with the strongest tendency to agglomerate.
- b) As a second series of experiments, TEM observations of these same aqueous additive suspensions were also performed. V-TiO₂ samples, with a lower particle size, presented larger and denser agglomerates of particles as clearly observable in Fig. 8.
- c) The third series of experimental tests included the obtaining of particle size distributions in aqueous media of alkaline pH and high Ca²⁺ concentration with the aim of mimicking the conditions of the fresh mortars during the bulk addition (Fig. 9). The results confirm the previous determinations of zeta potential and TEM micrographs, with higher agglomerates detected for V-TiO₂ additive (with a significant tail of particle size above 1100 nm).
- d) Finally, SEM-EDS examination of the mortars clearly showed how the V-TiO₂ generated areas with strong agglomeration of the particles. Elemental mapping indicate a homogeneous distribution of the Fe-TiO₂ additive within the binding matrices (Figure 10 shows air lime and Fig. 11 PC mortars), traceable by the Ti elemental mapping. However, for V-TiO₂ additive a clear accumulation of Ti and V in some specific areas was seen in both types of mortars (in Fig. 10 and

11, Ti and V elemental mapping showed matching brighter spots, as indicated by white arrows). These agglomerates reduced the active sites and resulted in spots of high recombination electron-hole pairs, reducing their lifetime and, subsequently, the NO_x removal. For mortars with Fe-TiO₂, the more homogeneous distribution of the photocatalyst accounts for their better photocatalytic efficiency.

To sum up, the V-TiO₂ additive yielded a lower amount of active sites in the mortars, contributing to a generally lower PCO efficiency.

- 4) Finally, the percentage of dopant can have a certain influence on the catalytic activity. An excess of dopant can also offer recombination sites for electron-hole pairs. In the current work, the dopant percentage of vanadium (1%) was much higher than that of the iron (below 0.5%) according to the XRF results.

Considering the final DeNO_x ability in comparison to other DeNO_x values reported in the literature [72], these cementing matrices yielded significant amounts of NO removal under the three illumination conditions, with high selectivity response for NO abatement that involves good percentages of NO_x abatements. As a way of example, for depolluting pavements (a piece of concrete including a final active coating with higher percentage of catalyst) under UV irradiation, NO_x abatement ranged from 20 to 30% [73], so that the systems of the current work would be more efficient in terms of DeNO_x ability considering the lower obtaining costs and catalyst consumption. Under solar illumination, some of these matrices reached NO removal values up to 15% (reported values for powder additives ranged between 17 and 25% [57]), with just a maximum 2.5% of additive by weight of binder. Under strict visible light, some of the mortars modified with photocatalysts yielded NO abatement percentages up to 5% (values of ca. 2% to 20% for pure powdered additives have been reported under visible light) [59,74]. These results encourage addressing studies on other photocatalysts with higher visible light sensitivity.

3.3. Hydrophilicity of the mortars: water contact angles

The hydrophilicity of the samples as measured by the static WCA was assessed. This parameter could serve as indicator of the self-cleaning ability of these cementing matrices, since the lower the contact angles the more effective dirt-prevention of the mortars [75]. When incorporated to cementing systems, besides the properties of the additives, the chemical and mineralogical composition of the binder, its roughness as well as its pore size distribution, also have a strong influence on the wettability of the surface of the mortars. From the point of view of the environmental effectiveness of these mortars, a reduction in the contact angles of the surfaces would have two positive effects: on one hand, a reduction in the chemicals used for cleaning purposes and, on the other hand, the final removal of the PCO products (nitrates) by rain would increase the cyclability of the photocatalysts, releasing the final product from the active sites.

In the current work the WCA was assessed in the specimens under the different illumination sources (1 hour of exposition) (Fig. 12). Although the sharp roughness of the surface of the mortars limited the hydrophilicity, results showed that the presence of the photocatalysts reduced the WCA, thus increasing the wettability of the mortars. Final static WCA values were in line with those reported for samples with high surface roughness [16]. Under UV and visible light, the average reduction of the WCA was similar, around 21%, while a 19% of reduction was measured for mortars under solar light. Bare TiO_2 caused an average reduction of 25.9%, whereas for Fe-TiO_2 and V-TiO_2 percentages of reduction were lower: 18.8% and 16.6%, respectively. The strongest reduction was seen for LAC and PC mortars (WCA reductions of 24.5 and 23.7%, respectively). For air lime mortars, WCA could not be measured due to the large porosity of these specimens (as a matter of fact, water drops could not –as suspected– be stabilized on the surface). Experimental results proved that the presence of photocatalysts increased the hydrophilicity of the mortars under light exposure, which can be positive for the dirt-prevention ability of these materials.

4. Conclusions

Different mortars with photocatalysts in bulk have been prepared and their abilities to degrade atmospheric nitrogen oxides were studied under different light conditions. Lime and HAC

mortars, among all the tested samples, showed the best NO abatement percentages under UV, solar and visible lights. This fact has been related to the synergistic effect caused by the presence of significant amounts of calcium carbonate that reacts with nitric acid as final product of the NO photooxidation. The sensitivity towards visible light has been proven by the increase in NO removal percentages of the mortars with the doped additives (Fe-TiO₂ and V-TiO₂), being the Fe-TiO₂ the most effective.

Selectivity values for NO degradation were very high (well above 60% for HAC and air lime mortars) implying a low release rate of harmful NO₂, so that these mortars are very interesting as supporting materials for an effective removal of atmospheric nitrogen oxides. Doped additives under visible light irradiation also yielded very high values of selectivity.

Finally, mortars with photocatalysts showed a water contact angle reduction, which, together with the photocatalytic activity, might contribute improving their self-cleaning ability.

Acknowledgments

This work was funded by MINECO, under grant MAT2015-70728-P. The research leading to these results has received funding from "la Caixa" Banking Foundation. M. Pérez-Nicolás thanks the Friends of the University of Navarra, Inc., for a pre-doctoral grant.

References

1. S.D. Beevers, E. Westmoreland, M.C. de Jong, M.L. Williams, D.C. Carslaw, Trends in NO_x and NO₂ emissions from road traffic in Great Britain, *Atmos. Environ.* 54 (2012) 107-116.
2. A. Folli, C. Pade, T. B. Hansen, T. De Marco, D. E. Macphee, TiO₂ photocatalysis in cementitious systems: Insights into self-cleaning and depollution chemistry, *Cem. Concr. Res.* 42 (2012) 539-548.
3. D.E. Macphee, A. Folli, Photocatalytic concretes — The interface between photocatalysis and cement chemistry, *Cem. Concr. Res.* 85 (2016) 48-54.
4. C. Mendoza, A. Valle, M. Castellote, A. Bahamonde, M. Faraldos, TiO₂ and TiO₂-SiO₂ coated cement: Comparison of mechanic and photocatalytic properties, *Appl. Catal. B* 178 (2015) 155-164.
5. J. Chen, S. Kou, C. Poon, Photocatalytic cement-based materials: Comparison of nitrogen oxides and toluene removal potentials and evaluation of self-cleaning performance, *Build. Environ.* 46 (2011) 1827-1833.
6. D. Wang, Z. Leng, M. Hüben, M. Oeser, B. Steinauer, Photocatalytic pavements with epoxy-bonded TiO₂-containing spreading material, *Constr. Build. Mater.* 107 (2016) 44-51.
7. R. Sugrañez, J.I. Álvarez, M. Cruz-Yusta, I. Mármol, J. Morales, J. Vila, L. Sánchez, Enhanced photocatalytic degradation of NO_x gases by regulating the microstructure of mortar cement modified with titanium dioxide, *Build. Environ.* 69 (2013) 55-63.

8. F. Wang, G. Sun, W. Zhang, L. Yang, P. Liu, Performance of photocatalytic cementitious material: Influence of substrate surface microstructure, *Constr. Build. Mater.* 110 (2016) 175-181.
9. N. Bossa, P. Chaurand, C. Levard, D. Borschneck, H. Miche, J. Vicente, C. Geantet, O. Aguerre-Chariol, F. M. Michel, J. Rose, Environmental exposure to TiO₂ nanomaterials incorporated in building material, *Environ. Pollut.* 220 (2017) 1160-1170.
10. C. Cárdenas, J.I. Tobón, C. García, J. Vila, Functionalized building materials: Photocatalytic abatement of NO_x by cement pastes blended with TiO₂ nanoparticles, *Constr. Build. Mater.* 36 (2012) 820-825.
11. J. Chen, C. Poon, Photocatalytic construction and building materials: From fundamentals to applications, *Build. Environ.* 44 (2009) 1899-1906.
12. K. Guan, Relationship between photocatalytic activity, hydrophilicity and self-cleaning effect of TiO₂/SiO₂ films, *Surface and Coatings Technology*, 191 (2005) 155-160.
13. S. Banerjee, D.D. Dionysiou, S.C. Pillai, Self-cleaning applications of TiO₂ by photo-induced hydrophilicity and photocatalysis, *Appl. Catal. B-Environ.*, 176-177 (2015) 396-428.
14. X. Yan, R. Abe, T. Ohno, M. Toyofuku, B. Ohtani, Action spectrum analyses of photoinduced superhydrophilicity of titania thin films on glass plates, *Thin. Solid. Films.* 516 (2008) 5872-5876.
15. M. Miyauchi, N. Kieda, S. Hishita, T. Mitsuhashi, A. Nakajima, T. Watanabe, K. Hashimoto, Reversible wettability control of TiO₂ surface by light irradiation, *Surf. Sci.* 511 (2002) 401-407.
16. E. Quagliarini, F. Bondioli, G. Battista Goffredo, C. Cordoni, P. Munafò, Self-cleaning and depolluting stone surfaces: TiO₂ nanoparticles for limestone, *Constr. Build. Mater.* 37 (2012) 51-57.
17. C. Kapridaki, L. Pinho, M. J. Mosquera, P. Maravelaki-Kalaitzaki, Producing photoactive, transparent and hydrophobic SiO₂-crystalline TiO₂ nanocomposites at ambient conditions with application as self-cleaning coatings, *Appl. Catal. B-Environ.* 156-157 (2014) 416-427.
18. Q. Li, Q. Liu, B. Peng, L. Chai, H. Liu, Self-cleaning performance of TiO₂-coating cement materials prepared based on solidification/stabilization of electrolytic manganese residue, *Constr. Build. Mater.* 106 (2016) 236-242.
19. M. Janus, J. Zatorska, A. Czyżewski, K. Bubacz, E. Kusiak-Nejman, A. W. Morawski, Self-cleaning properties of cement plates loaded with N,C-modified TiO₂ photocatalysts, *Appl. Surf. Sci.* 330 (2015) 200-206.
20. J. Zhao, X. Yang, Photocatalytic oxidation for indoor air purification: a literature review, *Build. Environ.* 38 (2003) 645-654.
21. M. Hoffmann, S. Martin, W. Choi, D. Bahnemann, Environmental Applications of Semiconductor Photocatalysis, *Chem. Rev.* 95 (1995) 69-96.
22. C. Yu, D. Cai, K. Yang, J.C. Yu, Y. Zhou, C. Fan, Sol-gel derived S,I-codoped mesoporous TiO₂ photocatalyst with high visible-light photocatalytic activity, *J. Phys. Chem. Solids.* 71 (2010) 1337-1343.
23. T. Baozhu, L. Chunzhong, G. Feng, J. Haibo, H. Yanjie, Z. Jinlong, Flame sprayed V-doped TiO₂ nanoparticles with enhanced photocatalytic activity under visible light irradiation, *Chem. Eng. J.* 151 (2009) 220-227.
24. I.A. Perales-Martínez, V. Rodríguez-González, S. Lee, S. Obregón, Facile synthesis of InVO₄/TiO₂ heterojunction photocatalysts with enhanced photocatalytic properties under UV-vis irradiation, *J. Photoch. Photobio. A.* 299 (2015) 152-158.
25. S. Wang, J.S. Lian, W.T. Zheng, Q. Jiang, Photocatalytic property of Fe doped anatase and rutile TiO₂ nanocrystal particles prepared by sol-gel technique, *Appl. Surf. Sci.* 263 (2012) 260-265.
26. M. Pelaez, N. T. Nolan, S. C. Pillai, M. K. Seery, P. Falaras, A. G. Kontos, P.S.M. Dunlop, J. W.J. Hamilton, J.A. Byrne, K. O'Shea, M. H. Entezari, D. D. Dionysiou, A review on the visible light active titanium dioxide photocatalysts for environmental applications, *Appl. Catal. B* 125 (2012) 331-349.
27. S. N. R. Inturi, T. Boningari, M. Suidan, P. G. Smirniotis. Visible-light-induced photodegradation of gas phase acetonitrile using aerosol-made transition metal (V, Cr, Fe, Co, Mn, Mo, Ni, Cu, Y, Ce, and Zr) doped TiO₂, *Appl. Catal. B* 144 (2014) 333-342.
28. M. Pérez-Nicolás, J. Balbuena, M. Cruz-Yusta, L. Sánchez, I. Navarro-Blasco, J.M. Fernández, J.I. Alvarez, Photocatalytic NO_x abatement by calcium aluminate cements modified with TiO₂: Improved NO₂ conversion, *Cem. Concr. Res.* 70 (2015) 67-76.
29. A. Izaguirre, J. Lanas, J.I. Alvarez, Effect of water-repellent admixtures on the behaviour of aerial lime-based mortars, *Cem. Concr. Res.* 39 (2009) 1095-1104.

30. J. Grilo, P. Faria, R. Veiga, A. Santos Silva, V. Silva, A. Velosa, New natural hydraulic lime mortars – Physical and microstructural properties in different curing conditions, *Constr. Build. Mater.* 54 (2014) 378-384.
31. L.C. Azeiteiro, A. Velosa, H. Paiva, P.Q. Mantas, V.M. Ferreira, R. Veiga, Development of grouts for consolidation of old renders, *Constr. Build. Mater.* 50 (2014) 352-360.
32. I. Karatasios, M. S. Katsiotis, V. Likodimos, A. I. Kontos, G. Papavassiliou, P. Falaras, V. Kilikoglou, Photo-induced carbonation of lime-TiO₂ mortars, *Appl. Catal. B* 95 (2010) 78-86.
33. J. Ângelo, L. Andrade, A. Mendes, Highly active photocatalytic paint for NO_x abatement under real-outdoor conditions, *Appl. Catal. A* 484 (2014) 17-25.
34. H. Derikvandi, A. Nezamzadeh-Ejhi, Synergistic effect of p-n heterojunction, supporting and zeolite nanoparticles in enhanced photocatalytic activity of NiO and SnO₂, *J. Colloid. Interf. Sci.* 490 (2017) 314-327.
35. X. Liu, B. Liang, M. Zhang, Y. Long, W. Li, Enhanced photocatalytic properties of α-SnWO₄ nanosheets modified by Ag nanoparticles, *J. Colloid. Interf. Sci.* 490 (2017) 46-52.
36. EN 459-1. Building lime. Part 1: definition, specification and conformity criteria, European Committee for Standardization, 2011.
37. I. Navarro-Blasco, A. Duran, R. Sirera, J.M. Fernández, J.I. Alvarez, Solidification/stabilization of toxic metals in calcium aluminate cement matrices, *J. Hazard. Mater.* 260 (2013) 89-103.
38. V. Etacheri, M. K. Seery, S. J. Hinder, S. C. Pillai, Highly Visible Light Active TiO₂-x Nx, Heterojunction Photocatalysts, *Chem. Mater.* 22 (2010) 3843-3853.
39. M. Kang, The superhydrophilicity of Al-TiO₂ nanometer sized material synthesized using a solvothermal method, *Mater. Lett.* 59 (2005) 3122-3127.
40. J. C.-S. Wu, C. Chen, A visible-light response vanadium-doped titania nanocatalyst by sol-gel method, *J. Photoch. Photobio. A*, 163 (2004) 509-515.
41. J.Ph. Nogier, M. Delamar, Chapter 7.1 X-ray photoelectron spectroscopy of TiO₂/V₂O₅ catalysts, *Catal. Today* 20 (1994) 109-123.
42. T. Chen, H. Lin, B. Guan, X. Gong, K. Li, Z. Huang, Promoting the low temperature activity of Ti-V-O catalysts by premixed flame synthesis, *Chem. Eng. J.* 296 (2016) 45-55.
43. A. Vittadini, M. Casarin, M. Sambri, A. Selloni, First-Principles Studies of Vanadia-Titania Catalysts: Beyond the Monolayer, *J. Phys. Chem. B* 109 (2005) 21766-21771.
44. B. Schimmoeller, R. Delaigle, D. P. Debecker, E. M. Gaigneaux, Flame-made vs. wet-impregnated vanadia/titania in the total oxidation of chlorobenzene: Possible role of VO_x species, *Catal. Today* 157 (2010) 198-203.
45. S. Li, Y. Ren, P. Biswas, S.D. Tse, Flame aerosol synthesis of nanostructured materials and functional devices: Processing, modeling, and diagnostics, *Prog. Energ. Combust.* 55 (2016) 1-59.
46. B. Schimmoeller, H. Schulz, A. Ritter, A. Reitzmann, B. Kraushaar-Czarnetzki, A. Baiker, S. E. Pratsinis, Structure of flame-made vanadia/titania and catalytic behavior in the partial oxidation of o-xylene, *J. Catal.* 256 (2008) 74-83.
47. G. Busca, L. Lietti, G. Ramis, F. Berti, Chemical and mechanistic aspects of the selective catalytic reduction of NO_x by ammonia over oxide catalysts: A review, *Appl. Catal. B* 18 (1998) 1-36.
48. N. Erdogan, J. Park, A. Ozturk, Synthesis and enhanced photocatalytic activity of molybdenum, iron, and nitrogen triple-doped titania nanopowders, *Ceram. Int.* 42 (2016) 16766-16774.
49. M. Crişan, M. Răileanu, N. Drăgan, D. Crişan, A. Ianculescu, I. Niţoi, P. Oancea, S. Şomărescu, N. Stănică, B. Vasile, C. Stan, Sol-gel iron-doped TiO₂ nanopowders with photocatalytic activity, *Appl. Catal. A* 504 (2015) 130-142.
50. EN 1015-19. Methods of Test for Mortar for Masonry. Part 9: Determination of Workable Life and Correction Time of Fresh Mortar Standardization, European Committee for Standardization, 2000.
51. ISO 22197-1. Test Method for Air Purification Performance of Semiconducting Photocatalytic Materials. Part 1: Removal of Nitric Oxide, International Organization for Standardization, 2007.
52. T. Martinez, A. Bertron, E. Ringot, G. Escadeillas, Degradation of NO using photocatalytic coatings applied to different substrates, *Build. Environ.* 46 (2011) 1808-1816.
53. M. P. Corrêa, Solar ultraviolet radiation: properties, characteristics and amounts observed in Brazil and South America, *An Bras Dermatol.* 90 (2015) 297-310.

54. Z.Ai, L. Zhu, S. Lee, L. Zhang, NO treated TiO₂ as an efficient visible light photocatalyst for NO removal, *J. Hazard. Mater.* 192 (2011) 361-367.
55. S.S. Lucas, V.M. Ferreira, J.L. Barroso de Aguiar, Incorporation of titanium dioxide nanoparticles in mortars — Influence of microstructure in the hardened state properties and photocatalytic activity, *Cem. Concr. Res.* 43 (2013) 112-120.
56. N. H. Nguyen, H. Bai, Photocatalytic removal of NO and NO₂ using titania nanotubes synthesized by hydrothermal method, *J. Environ. Sci.* 26 (2014) 1180-1187.
57. Y. Huang, W. Ho, S. Lee, L. Zhang, G. Li, J. C. Yu, Effect of Carbon Doping on the Mesoporous Structure of Nanocrystalline Titanium Dioxide and its Solar-Light-Driven Photocatalytic Degradation of NO_x, *Langmuir* 24 (2008) 3510-3516.
58. N. S. Allen, M.Edge, J. Verran, J. Stratton, J. Maltby, C. Bygott, Photocatalytic titania based surfaces: Environmental benefits, *Polym. Degrad. Stabil.* 93 (2008) 1632-1646.
59. I. Papailias, N. Todorova, T. Giannakopoulou, J. Yu, D. Dimotikali, C. Trapalis, Photocatalytic activity of modified g-C₃N₄/TiO₂ nanocomposites for NO_x removal, *Catal. Today* 280 (2017) 37-44.
60. M. Nuño, G. L. Pesce, C. R. Bowen, P. Xenophontos, R. J. Ball, Environmental performance of nano-structured Ca(OH)₂/TiO₂ photocatalytic coatings for buildings, *Build. Environ.* 92 (2015) 734-742.
61. J. Balbuena, G. Carraro, M. Cruza, A. Gasparotto, C. Maccato, A. Pastora, C. Sada, D. Barreca, L. Sánchez, Advances in photocatalytic NO_x abatement through the use of Fe₂O₃/TiO₂ nanocomposites, *RSC. Adv.* 6 (2016) 74878-74885.
62. A. Strini, G. Roviello, L. Ricciotti, C. Ferone, F. Messina, L. Schiavi, D. Corsaro, R. Cioffi, TiO₂-Based Photocatalytic Geopolymers for Nitric Oxide Degradation, *Materials* 9 (2016) 513.
63. T. Giannakopoulou, N. Todorova, G. Romanos, T. Vaimakis, R. Dillert, D. Bahnemann, C. Trapalis, Composite hydroxyapatite/TiO₂ materials for photocatalytic oxidation of NO_x, *Mater Sci. Eng., B* 177 (2012) 1046-1052.
64. S. Martínez, F. Acción, F. Puertas, Characterization of alkali-metal and alkaline-earth nitrates by vibrational spectroscopy, *Mater. Construcc.* 42 (1992) 25-36.
65. A.K. Maier, L. Dezmirean, J. Will, P. Greil, Three-dimensional printing of flash-setting calcium aluminate cement, *J. Mater. Sci.* 46 (2011) 2947-2954.
66. S. Thangavel, K. Krishnamoorthy, V. Krishnaswamy, N. Raju, S. J. Kim, G. Venugopal, Graphdiyne-ZnO Nanohybrids as an Advanced Photocatalytic Material, *J. Phys. Chem. C* 119 (2015) 22057-22065.
67. S. Klosek, D. Raftery, Visible light driven V-doped TiO₂ photocatalyst and its photooxidation of ethanol, *J. Phys. Chem. B* 105 (2001) 2815-2819.
68. W. Choi, A. Termin, M. R. Hoffmann, Metal Ion Dopants in Quantum-Sized TiO₂, *J. Phys. Chem.* 98 (1994) 13669-13679.
69. N. Todorova, T. Vaimakis, D. Petrakis, S. Hishita, N. Boukos, T. Giannakopoulou, M. Giannouri, S. Antiohos, D. Papageorgiou, E. Chaniotakis, C. Trapalis, N and N,S-doped TiO₂ photocatalysts and their activity in NO_x oxidation, *Catal. Today* 209 (2013) 41-46.
70. M.M. Ballari, M. Hunger, G. Hüsken, H.J.H. Brouwers, Modelling and experimental study of the NO_x photocatalytic degradation employing concrete pavement with titanium dioxide, *Catal. Today* 151 (2010) 71-76.
71. M. Kang, Synthesis of Fe/TiO₂ photocatalyst with nanometer size by solvothermal method and the effect of H₂O addition on structural stability and photodecomposition of methanol, *J. Mol. Catal. A: Chem.* 197 (2003) 173-183.
72. A. Trapalis, N. Todorova, T. Giannakopoulou, N. Boukos, T. Speliotis, D. Dimotikali, J. Yu, TiO₂/graphene composite photocatalysts for NO_x removal: A comparison of surfactant-stabilized graphene and reduced graphene oxide, *Appl. Catal. B-Environ.* 180 (2016) 637-647.
73. M.M. Ballari, M. Hunger, G. Hüsken, H.J.H. Brouwers, NO_x photocatalytic degradation employing concrete pavement containing titanium dioxide, *Appl. Catal. B-Environ.* 95 (2010) 245-254.
74. H. Nie, M. Ou, Q. Zhong, S. Zhang, L. Yu, Efficient visible-light photocatalytic oxidation of gaseous NO with graphitic carbon nitride (g-C₃N₄) activated by the alkaline hydrothermal treatment and mechanism analysis, *J. Hazard. Mater.* 300 (2015) 598-606.
75. J. Wang, H. Tsai, J. Uan, M. Wong, S. Wu, Investigation of the photo-catalytic coating on AZ91 alloy, *J. Alloys Compd.* 467 (2009) 257-260.

Table 1. Chemical and mineralogical compositions of the raw cementing phases.

<i>Binding phase</i>	<i>Al₂O₃</i> (%)	<i>CaO</i> (%)	<i>Fe₂O₃</i> (%)	<i>SiO₂</i> (%)	<i>SO₃</i> (%)	<i>Na₂O</i> + <i>K₂O</i> (%)	<i>Main mineralogical phases</i>	<i>Minor mineralogical phases</i>
<i>PC</i>	4.0	62.0	4.0	20.0	1.6	0.3	Ca ₃ SiO ₅ (C ₃ S), Ca ₂ SiO ₄ (C ₂ S)	Ca ₃ Al ₂ O ₆ (C ₃ A), Ca ₄ Al ₂ Fe ₂ O ₁₀ (C ₄ AF), CaSO ₄
<i>HAC</i>	70.5	28.5	0.2	0.6	<0.3	<0.5	CaAl ₂ O ₄ , (CA), CaAl ₄ O ₈ (CA ₂)	Ca ₁₂ Al ₁₄ O ₃₃ (C ₁₂ A ₇), CaCO ₃ (C)
<i>LAC</i>	41.5	38.0	10.5	3.0	0.1	0.1	CaAl ₂ O ₄ (CA)	Ca ₂ FeAlO ₅ (C ₄ AF), Ca ₁₂ Al ₁₄ O ₃₃ (C ₁₂ A ₇), β-Ca ₂ SiO ₄ (C ₂ S), Ca ₃ TiFe ₂ O ₈ , FeO
<i>Air lime</i>	0.4	68.5	0.5	1.03	1.4	0.14	Ca(OH) ₂ (P)	CaCO ₃ (C)

Table 2. Characteristics of the photocatalytic additives.

<i>Photocatalytic additive</i>	<i>Particle size</i> (nm)	<i>Density</i> (g cm ⁻³)	<i>Specific Surface area</i> (m ² g ⁻¹)	<i>Anatase</i> (%)	<i>Rutile</i> (%)
<i>TiO₂</i> *	21	4.26	50	78.8	21.2
<i>Fe- TiO₂</i>	16	3.90	101	69.1	30.9
<i>V- TiO₂</i>	15	3.38	113	77.5	22.5

*Density and particle size according to data provided by the supplier

Table 3. Selectivity values (ratios of NO_x/NO removal in percentage) of all tested binding matrices under UV, solar and visible irradiation.

<i>Ultraviolet light</i>							
		<i>PC</i>	<i>LAC cured 20 °C</i>	<i>LAC cured 60 °C</i>	<i>HAC cured 20 °C</i>	<i>HAC cured 60 °C</i>	<i>Air lime</i>
<i>TiO₂</i>	<i>0.5%</i>	47.7	49.5	45.9	74.3	60.8	72.8
	<i>1.0%</i>	47.8	63.6	51.8	77.7	58.6	75.5
	<i>2.5%</i>	69.5	67.5	61.0	78.7	69.5	80.8
<i>Fe-TiO₂</i>	<i>0.5%</i>	53.0	51.0	53.4	63.9	65.1	62.8
	<i>1.0%</i>	43.1	52.5	50.1	61.3	66.3	77.1
	<i>2.5%</i>	65.6	57.3	61.9	68.3	71.0	78.4
<i>V-TiO₂</i>	<i>0.5%</i>	43.9	44.4	45.1	62.0	67.5	54.0
	<i>1.0%</i>	50.3	46.4	44.5	66.1	60.7	66.5
	<i>2.5%</i>	54.1	57.3	57.7	69.3	60.7	76.7

<i>Solar light</i>							
		<i>PC</i>	<i>LAC cured 20 °C</i>	<i>LAC cured 60 °C</i>	<i>HAC cured 20 °C</i>	<i>HAC cured 60 °C</i>	<i>Air lime</i>
<i>TiO₂</i>	<i>0.5%</i>	59.0	71.1	33.3	83.5	79.0	82.2
	<i>1.0%</i>	60.3	59.4	47.0	79.8	77.9	82.4
	<i>2.5%</i>	63.2	76.8	60.1	85.1	80.3	79.4
<i>Fe-TiO₂</i>	<i>0.5%</i>	51.7	77.9	30.3	78.5	72.9	81.8
	<i>1.0%</i>	48.0	62.9	59.6	77.9	74.2	85.0
	<i>2.5%</i>	54.7	55.1	60.2	76.2	78.1	79.3
<i>V-TiO₂</i>	<i>0.5%</i>	39.6	59.7	35.2	79.0	58.3	67.3
	<i>1.0%</i>	17.4	73.4	41.5	48.8	71.2	76.7
	<i>2.5%</i>	36.2	70.9	81.0	67.8	84.5	80.6

<i>Visible light</i>							
		<i>PC</i>	<i>LAC cured 20 °C</i>	<i>LAC cured 60 °C</i>	<i>HAC cured 20 °C</i>	<i>HAC cured 60 °C</i>	<i>Air lime</i>
<i>TiO₂</i>	<i>0.5%</i>	80.8	70.6	66.0	70.4	78.1	63.1
	<i>1.0%</i>	62.2	83.9	69.9	72.6	65.3	71.4
	<i>2.5%</i>	70.7	87.7	82.4	44.5	65.5	77.1
<i>Fe-TiO₂</i>	<i>0.5%</i>	44.9	77.1	76.7	77.9	78.1	82.5
	<i>1.0%</i>	61.4	85.9	76.4	63.2	57.8	82.2
	<i>2.5%</i>	72.1	79.6	73.1	71.3	68.9	86.1
<i>V-TiO₂</i>	<i>0.5%</i>	72.2	76.2	84.8	76.4	65.9	50.9
	<i>1.0%</i>	83.9	82.5	77.9	80.2	76.1	74.3
	<i>2.5%</i>	84.5	72.6	85.1	80.8	73.8	82.2

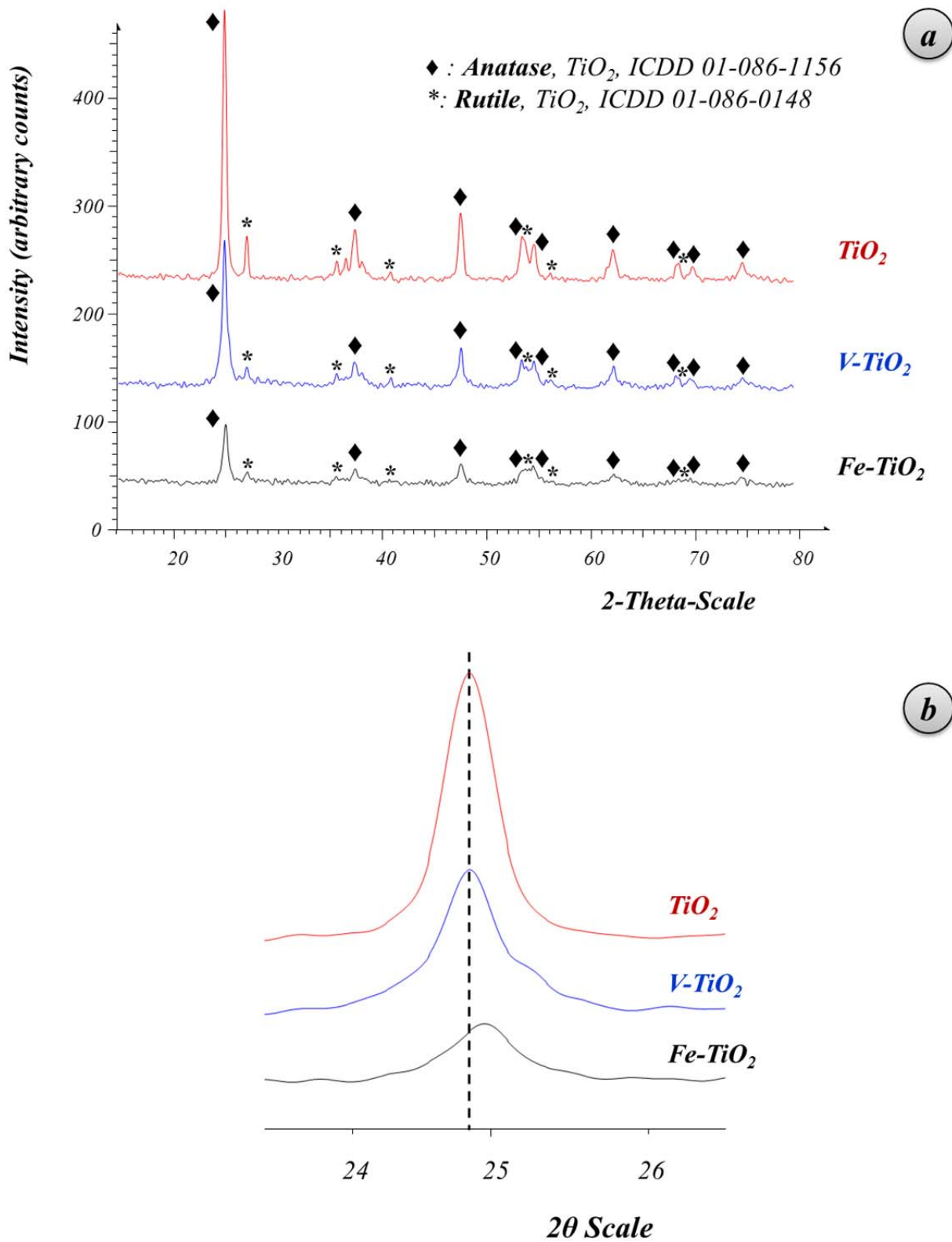


Figure 1. a) XRD patterns of the three photocatalytic additives. b) XRD detail of the (1 0 1) peak of the anatase for bare TiO_2 , V-TiO_2 and Fe-TiO_2 .

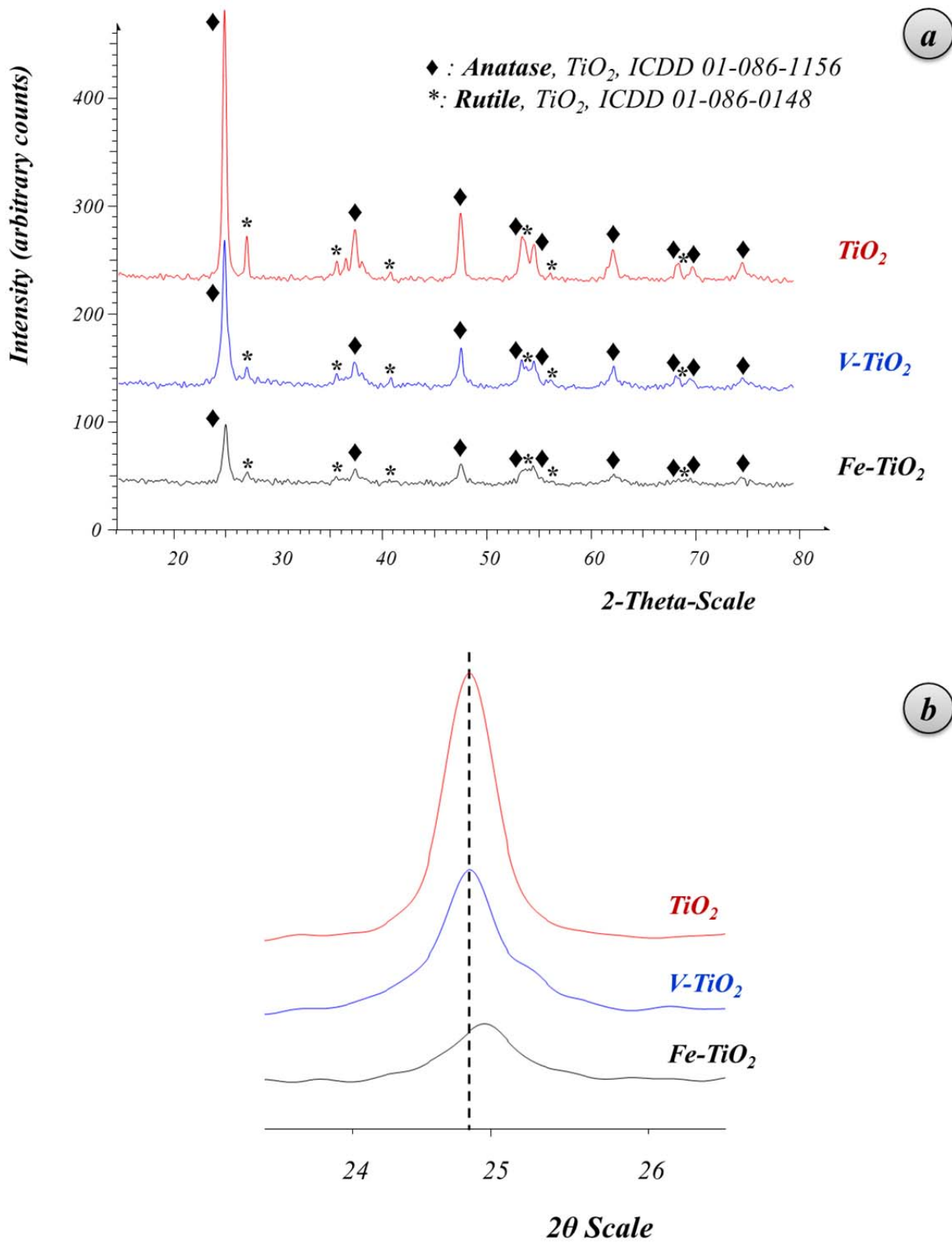


Figure 1. a) XRD patterns of the three photocatalytic additives. b) XRD detail of the (1 0 1) peak of the anatase for bare TiO_2 , V-TiO_2 and Fe-TiO_2 .

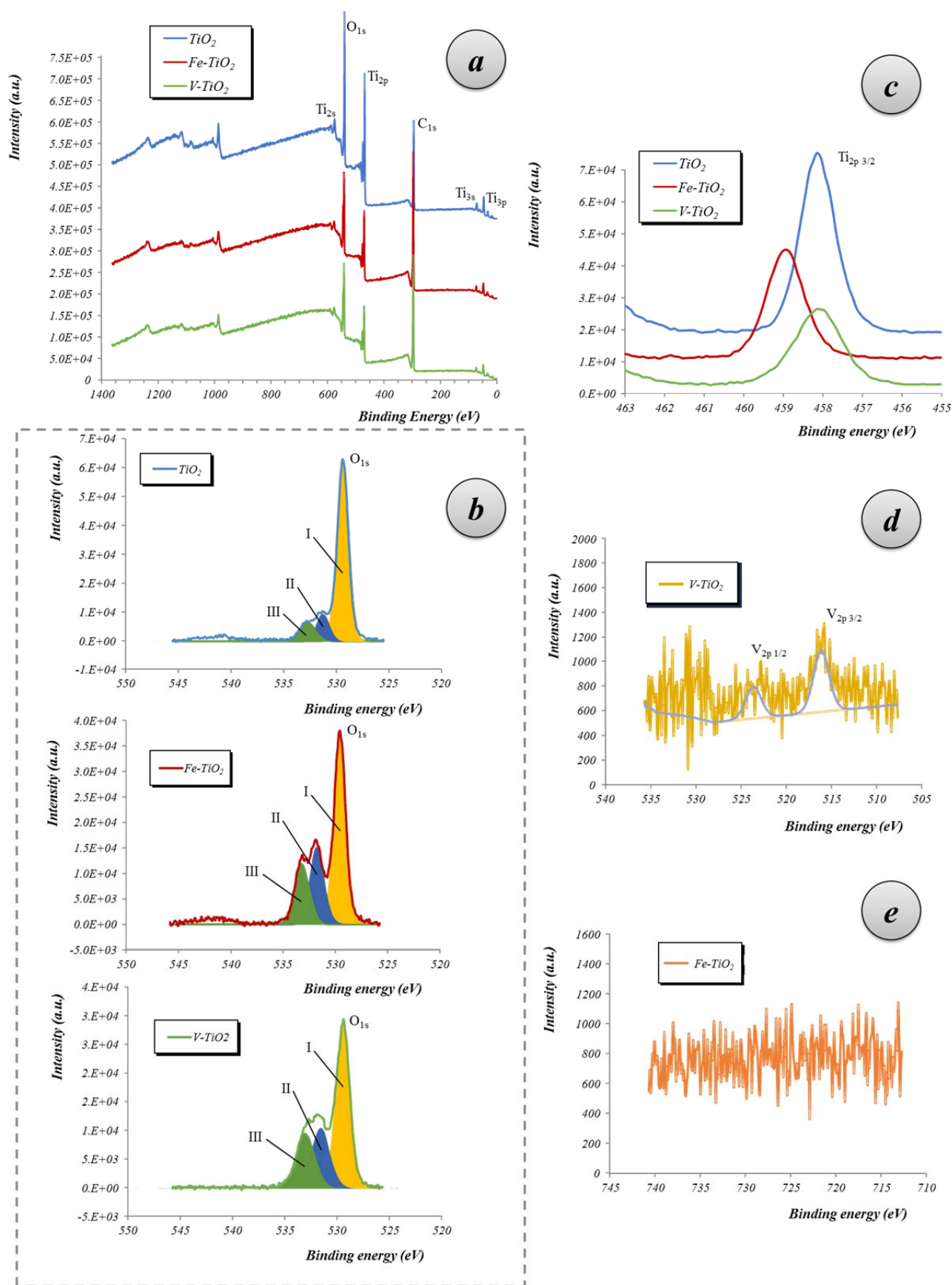


Figure 2. XPS results of the photocatalysts: a) survey spectra; b) O region; c) Ti region, d) V region for the V- TiO_2 sample; e) Fe region of the Fe- TiO_2 catalyst.

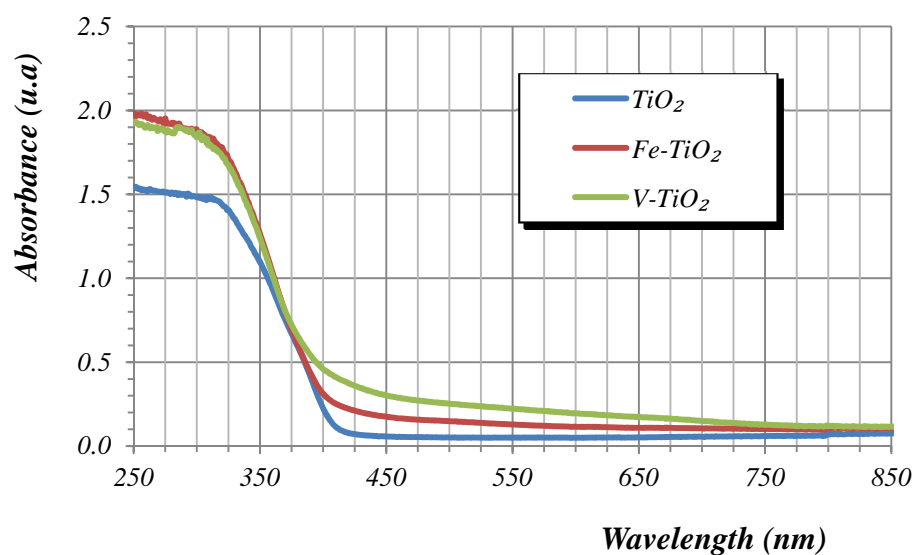


Figure 3. UV-vis diffuse reflectance spectra of the three photocatalysts.

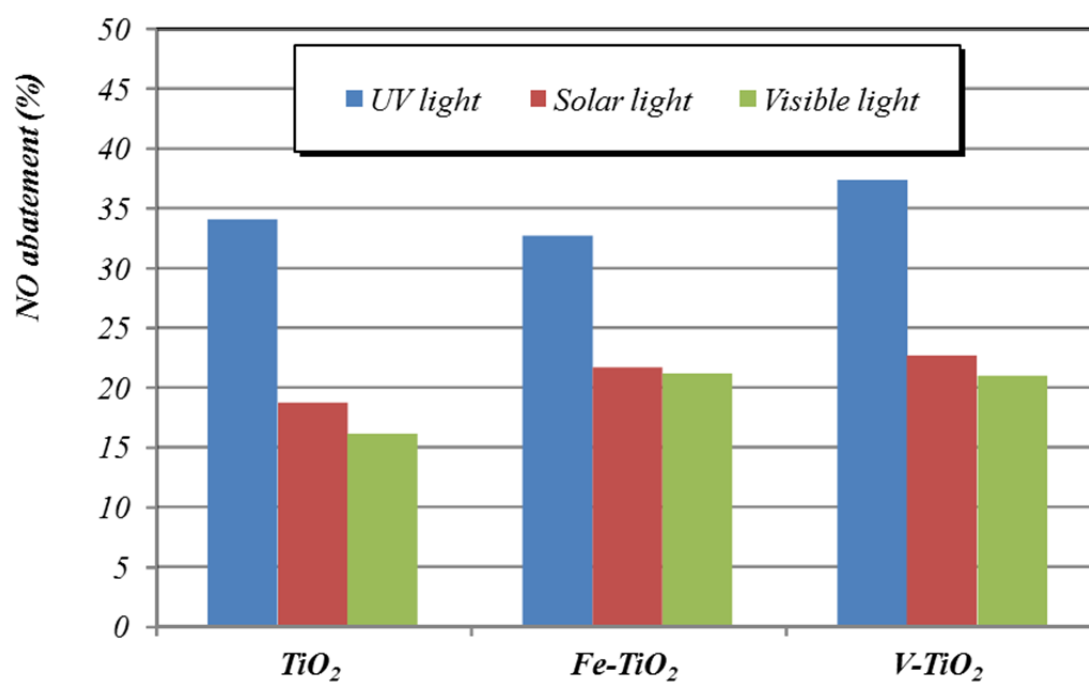


Figure 4. NO abatements for powder photocatalytic additives under different illumination sources.

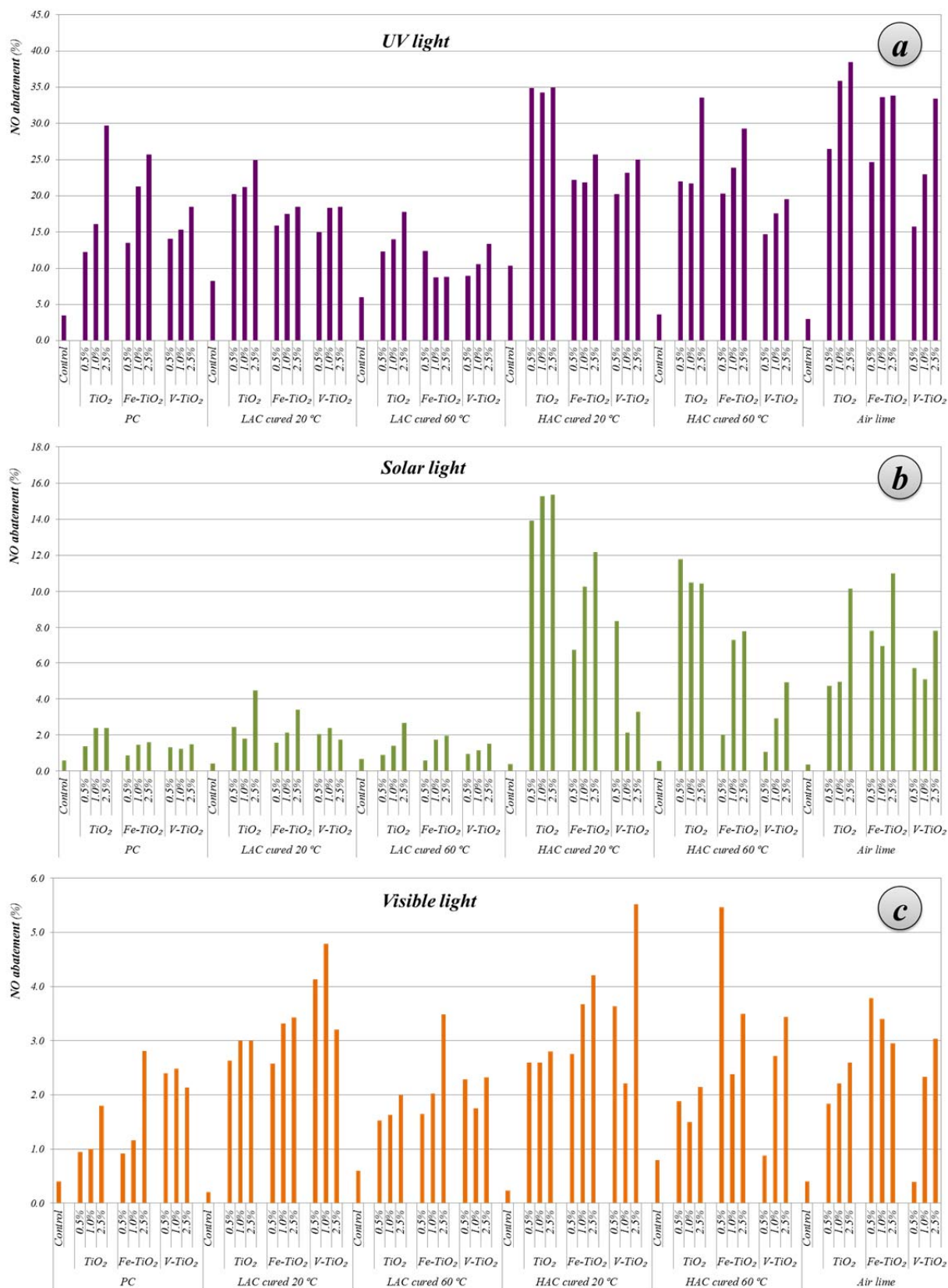


Figure 5. Percentages of nitric oxide PCO removal by different additives included in different cementing matrices studied under: a) UV light; b) solar light; c) visible light.

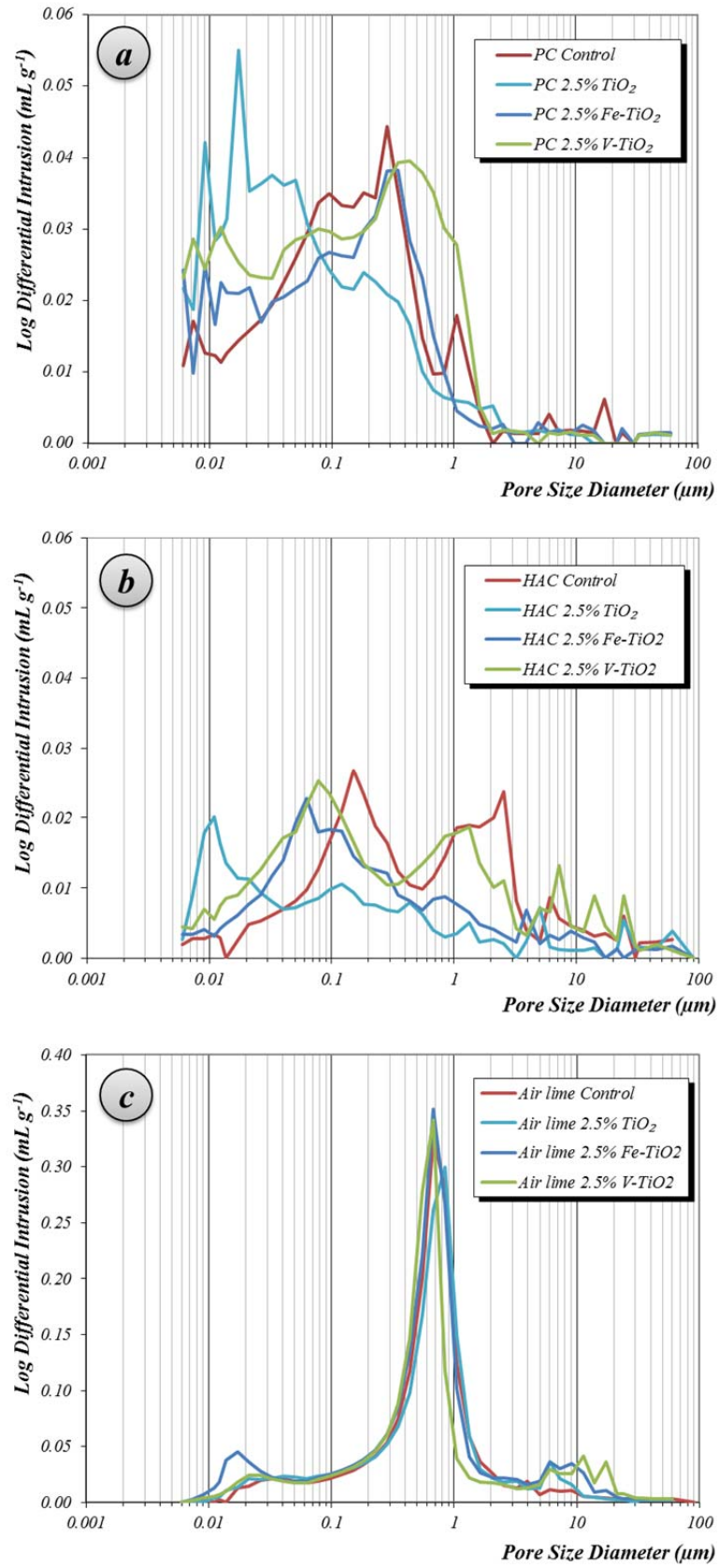


Figure 6. Pore size distribution of a) PC- b) HAC- c) air lime- mortars with photocatalysts after 28 curing days.

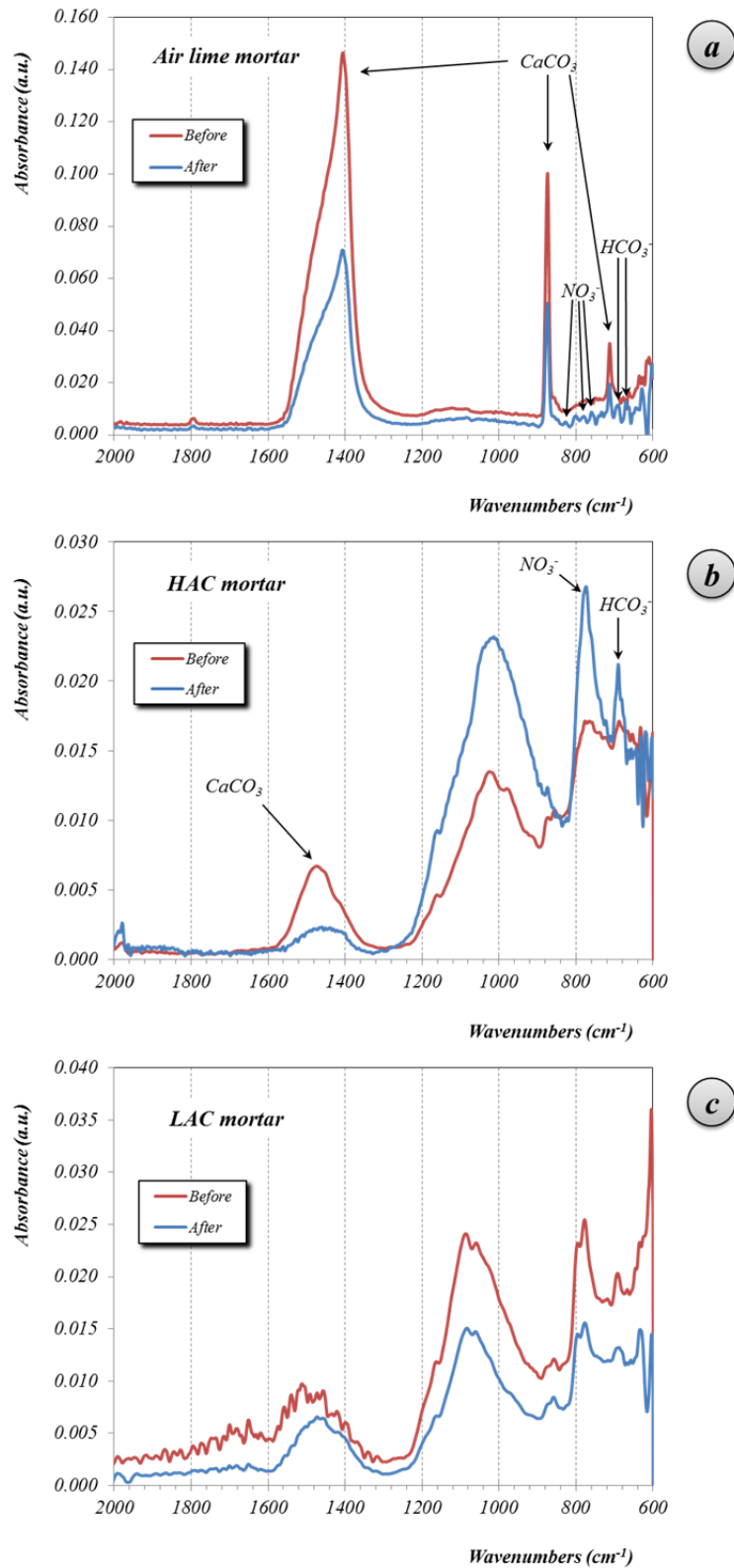


Figure 7. FTIR results of mortars (2.5% of TiO_2) before and after the exposure to NO flow for 2 h: a) air lime mortars, b) HAC mortars and c) LAC mortars. Absorption bands of some relevant compounds are indicated.

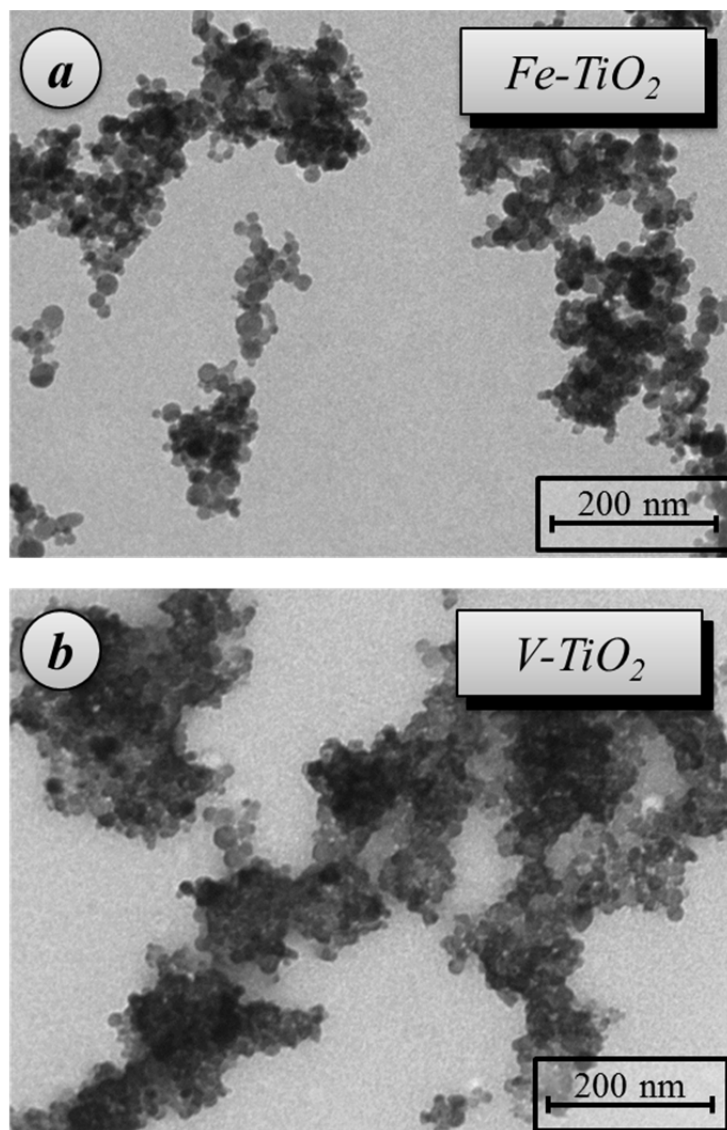


Figure 8. TEM micrographs of (a) Fe-TiO₂ and (b) V-TiO₂ aqueous suspensions.

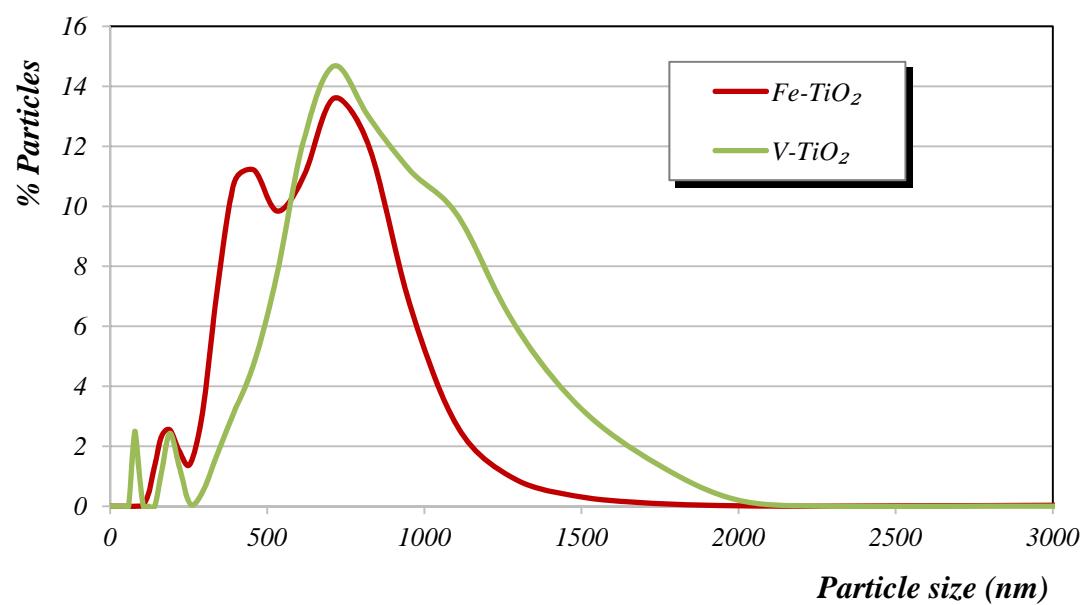


Figure 9. Particle size distribution of the doped additives at pH 12.5 in a CaCl₂ saturated medium.

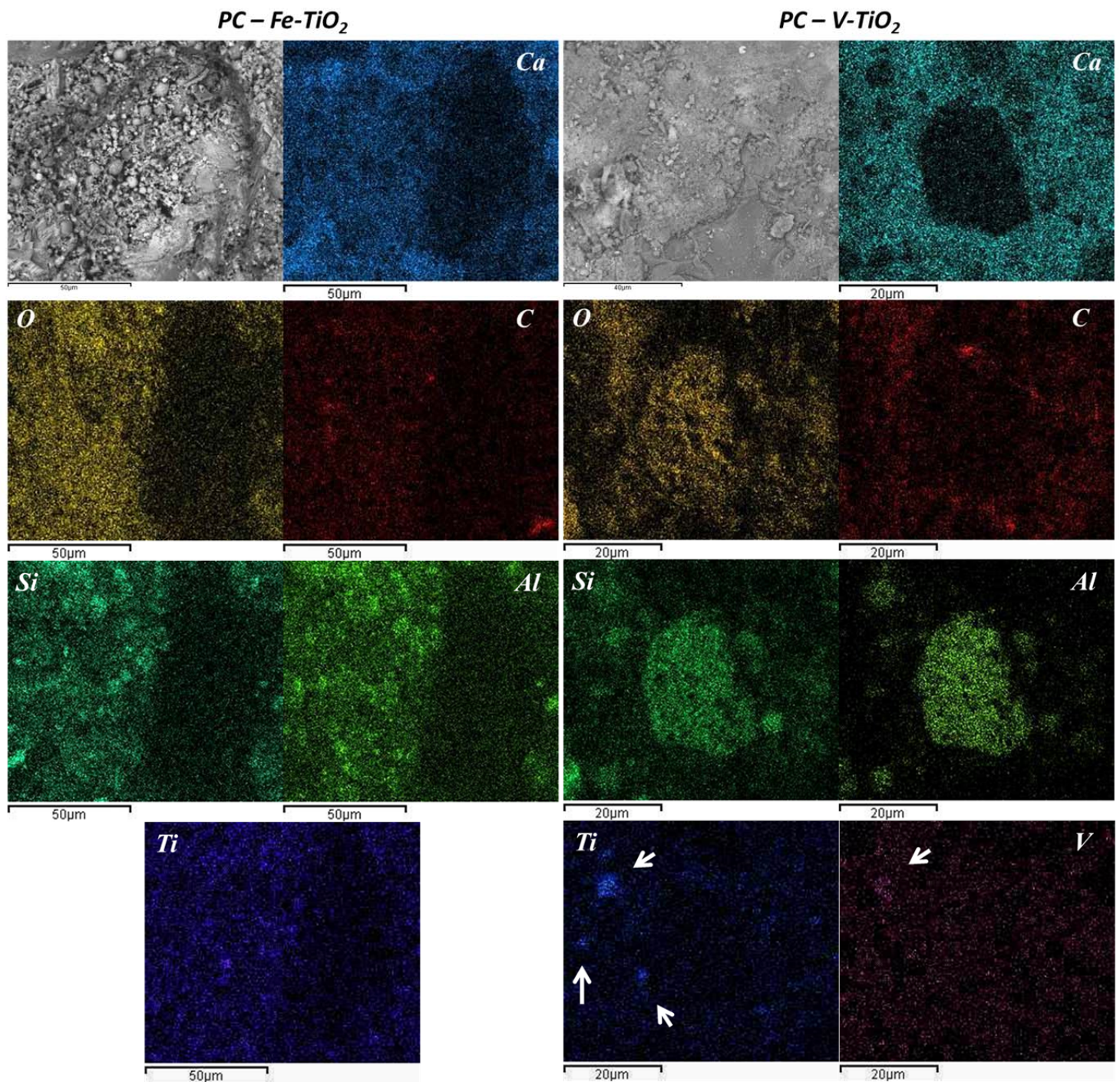


Figure 11. Elemental mapping of PC mortars with $Fe-TiO_2$ and $V-TiO_2$. White arrows indicate the brighter spots of accumulation of $V-TiO_2$.

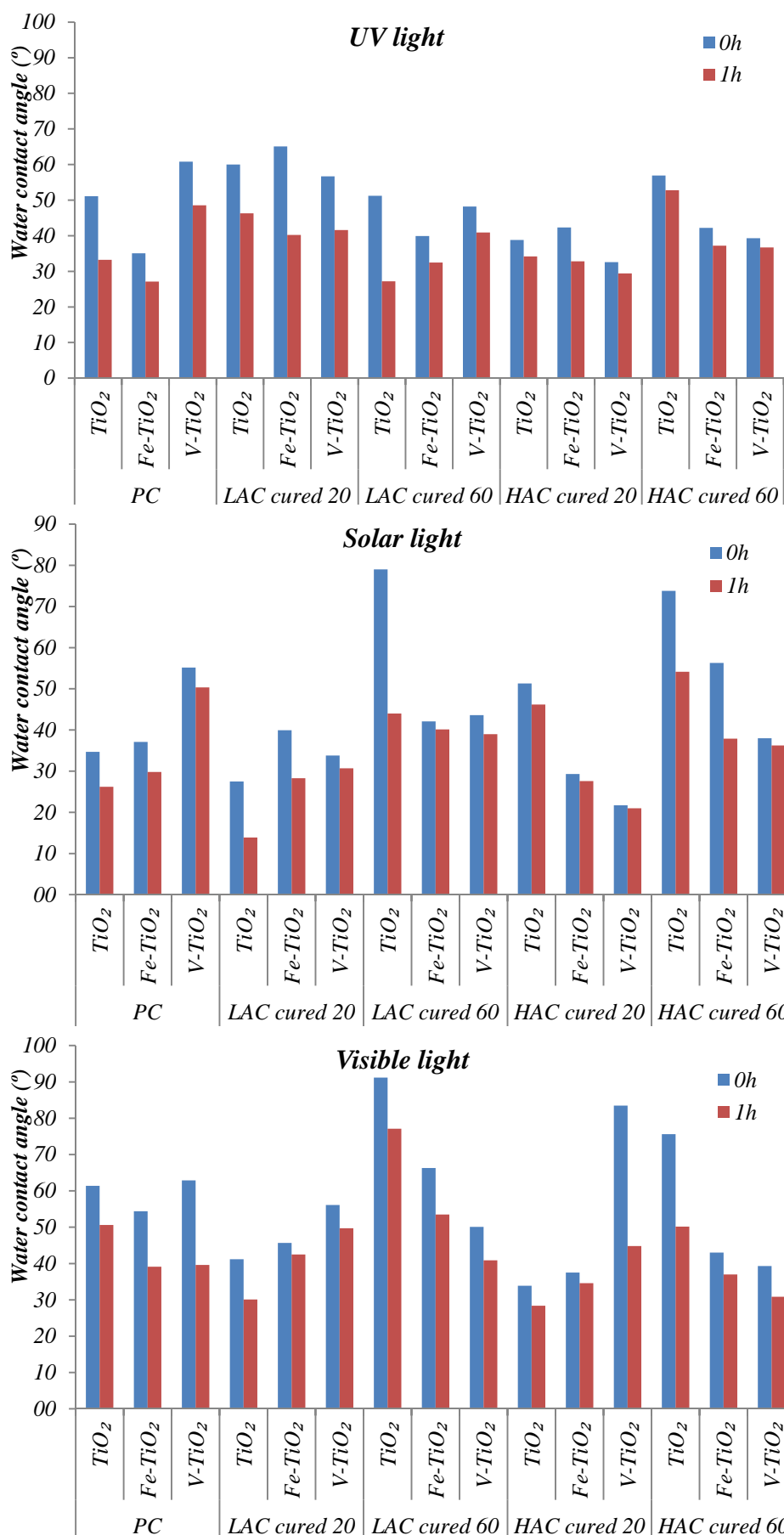


Figure 12. Static water contact angle for mortars with 2.5% of additive before (0 h) and after (1 h) UV, solar and visible light illumination.

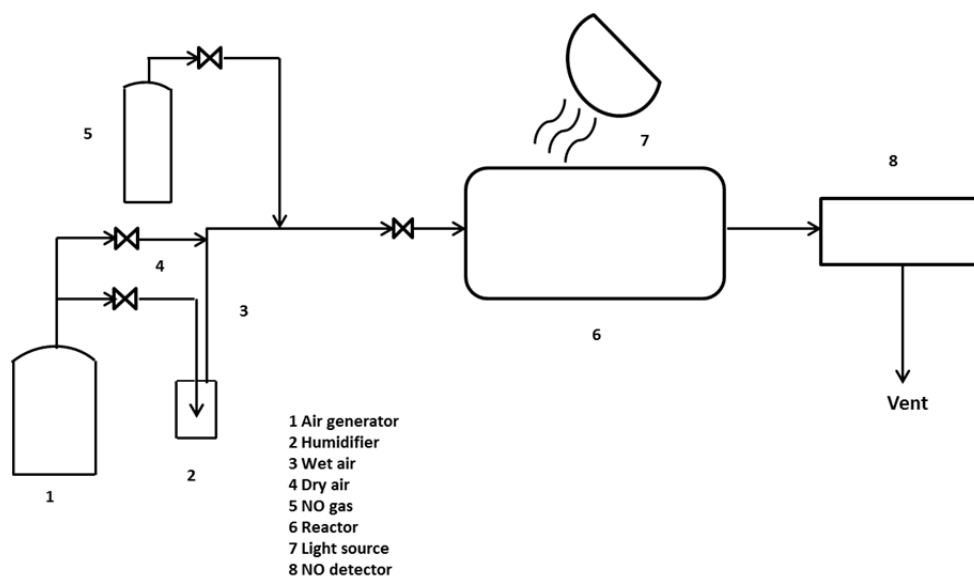


Figure S1. Scheme of the laminar flow reactor for photocatalytic measurements.

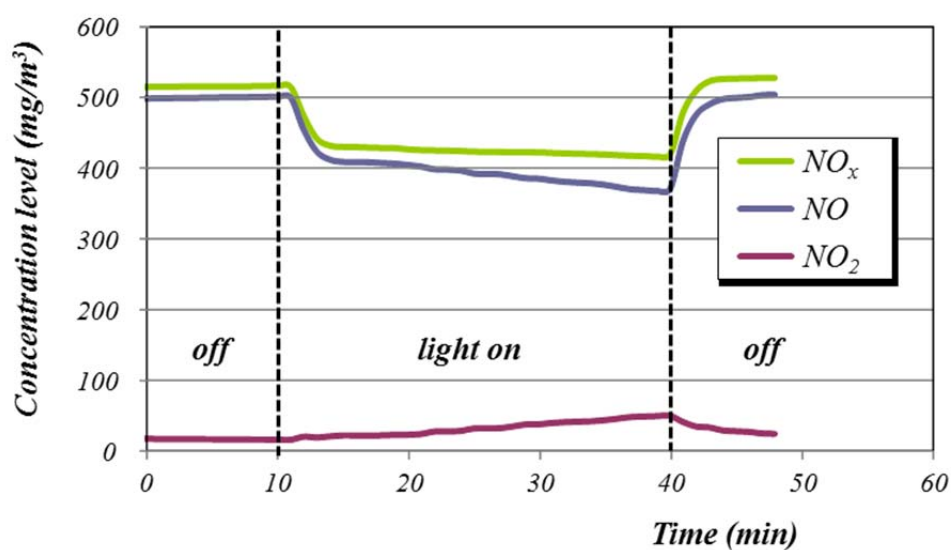


Figure S2. Experimental profiles of NO, NO₂ and NO_x concentrations during the photocatalytic tests of NO degradation.

Table S1. Values of the pseudo-first order kinetics constants corresponding to the NO abatements of all assayed binding matrices under UV, solar and visible irradiation.

Sample		Rate constant (min ⁻¹)				
		UV light	Solar light	Visible light		
PC	Control	0%	0.0045	0.0003	0.0002	
		0.5%	0.0230	0.0010	0.0007	
		1.0%	0.0086	0.0022	0.0017	
		2.5%	0.0329	0.0030	0.0039	
	TiO ₂	0.5%	0.0182	0.0004	0.0019	
		1.0%	0.0140	0.0008	0.0007	
		2.5%	0.0183	0.0004	0.0009	
	Fe-TiO ₂	0.5%	0.0165	0.0005	0.0005	
		1.0%	0.0255	0.0010	0.0004	
		2.5%	0.0403	0.0018	0.0028	
	V-TiO ₂	0.5%	0.0155	0.0004	0.0047	
		1.0%	0.0293	0.0004	0.0006	
		1.0%	0.0300	0.0005	0.0005	
		2.5%	0.0632	0.0031	0.0016	
LAC cured 20 °C	Fe-TiO ₂	0.5%	0.0275	0.0009	0.0010	
		1.0%	0.0192	0.0006	0.0004	
		2.5%	0.0144	0.0017	0.0030	
		0.5%	0.0276	0.0002	0.0009	
	V-TiO ₂	1.0%	0.0142	0.0007	0.0035	
		2.5%	0.0144	0.0005	0.0014	
		Control	0%	0.0061	0.0003	0.0005
	0.5%		0.0246	0.0005	0.0009	
	1.0%		0.0280	0.0006	0.0020	
	2.5%		0.0450	0.0002	0.0004	
	LAC cured 60 °C	Fe-TiO ₂	0.5%	0.0171	0.0022	0.0004
			1.0%	0.0154	0.0016	0.0005
2.5%			0.0212	0.0004	0.0003	
V-TiO ₂		0.5%	0.0126	0.0005	0.0019	
		1.0%	0.0203	0.0003	0.0003	
		2.5%	0.0239	0.0007	0.0010	
HAC cured 20 °C		Control	0%	0.0081	0.0006	0.0002
			0.5%	0.0873	0.0033	0.0020
			1.0%	0.1007	0.0174	0.0001
	2.5%		0.1136	0.0249	0.0003	
	TiO ₂	0.5%	0.0272	0.0020	0.0001	
		1.0%	0.0448	0.0072	0.0009	
		2.5%	0.0719	0.0039	0.0006	
	Fe-TiO ₂	0.5%	0.0481	0.0064	0.0006	
		1.0%	0.0600	0.0005	0.0013	
		2.5%	0.0351	0.0014	0.0004	
	V-TiO ₂	0.5%	0.0010	0.0003	0.0006	
		1.0%	0.0349	0.0147	0.0002	
		1.0%	0.0329	0.0174	0.0006	
		2.5%	0.0959	0.0132	0.0003	
HAC cured 60 °C	Control	0%	0.0010	0.0003	0.0006	
		0.5%	0.0349	0.0147	0.0002	
		1.0%	0.0329	0.0174	0.0006	
		2.5%	0.0959	0.0132	0.0003	
	TiO ₂	0.5%	0.0459	0.0002	0.0000	
		1.0%	0.0610	0.0008	0.0008	
		2.5%	0.1005	0.0042	0.0002	
	Fe-TiO ₂	0.5%	0.0329	0.0001	0.0006	
		1.0%	0.0410	0.0010	0.0004	
		2.5%	0.0550	0.0012	0.0005	
	V-TiO ₂	0.5%	0.0108	0.0006	0.0016	
		1.0%	0.0598	0.0110	0.0035	
1.0%		0.0825	0.0088	0.0066		
2.5%		0.1248	0.0091	0.0130		
Air lime	Control	0%	0.0108	0.0006	0.0016	
		0.5%	0.0598	0.0110	0.0035	
		1.0%	0.0825	0.0088	0.0066	
	TiO ₂	0.5%	0.0287	0.0104	0.0005	
		1.0%	0.0687	0.0072	0.0010	
		2.5%	0.0596	0.0113	0.0025	
	Fe-TiO ₂	0.5%	0.0287	0.0104	0.0005	
		1.0%	0.0687	0.0072	0.0010	
		2.5%	0.0596	0.0113	0.0025	
V-TiO ₂	0.5%	0.0119	0.0081	0.0019		
	1.0%	0.0263	0.0034	0.0014		
	2.5%	0.0508	0.0145	0.0053		